Characterizations of Deformable Mirror in a Sensorless Adaptive Optics System

Dong Shen

TUDelft Delft University of Technology

Delft Center for Systems and Control

Characterizations of Deformable Mirror in a Sensorless Adaptive Optics System

MASTER OF SCIENCE THESIS

For the degree of Master of Science in Systems and Control at Delft University of Technology

Dong Shen

May 23, 2023

Faculty of Mechanical, Maritime and Materials Engineering (3mE) · Delft University of Technology

Abstract

Deformable Mirror (DM) is the key part in the AO system. Characterization of DM is important as it maps between input voltage signal and output mirror deformation. The precision of characterization largely affects the control performance. While characterizing the DM with wavefront sensors is easy and straightforward, there is very few research on the characterizing the DM in a Wavefront sensorless (WFSless) setup. Existing research focuses on using Phase Diversity Phase Retrieval (PDPR) methods to retrieve phase, while introducing diversity phase by using various additional hardware.

This thesis tries to use PDPR methods to characterize the DM in a WFSless setup without using any additional hardware. Diversity phase are introduced by the DM itself and calibrated afterwards. Simulation results show that the proposed method is capable of characterizing the DM. Experiments on the setup are also conducted and further validates the proposed method, while unstable setup is accountable for the undesired results of the characterization.

Table of Contents

Chapter 1

Introduction

Adaptive Optics (AO) has been used in various fields including astronomy, microscopy, medical imaging and lithography manufacturing Ref[1][2]. AO systems can be with or without sensor for phase detection, while sensors can also be used for the calibration of DM actuators. In a Wavefront sensorless (WFSless) setup, no direct wavefront sensor is used. Sensorless AO is used more often than direct wavefront sensing in microscopy since the requirement of point-like source of light is hardly met in such applications Ref[1]. The key element in an AO setup is the Deformable Mirror (DM), which is used to correct aberrations and allow for high resolution images.

DMs correct aberrations by altering the phase of propagating beam. It can be also seen as DM generating a Wavefront (WF) that compensates for the original one. To control a DM, one typically needs to obtain a control matrix that links input voltage to the output deformation of the mirror surface Ref[3]. If the phase introduced by the DMs is known, it would be much easier to determine the control input.

In a WFSless setting, it is more challenging to obtain such control matrices as no sensor is used. One can of course bypass the problem of WF reconstruction by iteratively optimizing a certain metric function as in Ref[4] to obtain good control inputs, but the long process time and underlying nonlinearity are hard to tackle. A more recent model-based version of such closed-loop control strategy is making use of the linear relationship of mean square of the aberration gradient and the second moment of the image intensity distribution as in Ref[5].

By far, most DM control strategies heavily rely on the close-loop structure or iterative computation. A more direct way of controlling the DM is to reconstruct the wavefront from intensity measurements and then map between the change in wavefronts and DM inputs, so as to "characterize" the DM. Such characterization would allow for fast, accurate and even open-loop control of the DM. In this approach, phase reconstruction plays an important role and multiple phase-retrieval methods have been developed in the past Ref[6].

1-1 Research Question

As mentioned above, the aim of this project is to characterize the DM using reconstructed wavefronts. More specifically, let the phase of incoming aberrated wavefront be noted as ϕ, the phase change introduced by DM be noted by ϕ_c and the residual wavefront after DM be noted by ϕ_r, their relation can be described by:

$$\phi_r = \phi - \phi_c. \tag{1-1}$$

The only measurable output in the WFSless AO system is the point spread function(PSF) measured by focal plane sensors:

$$I(\zeta, \phi_r) = |\mathcal{F}(A(x)e^{i\phi_r(x)})|^2. \tag{1-2}$$

where $\zeta, x \in \mathbb{R}^2$ representing the image and pupil plane coordinates respectively and A represents the amplitude.
The change of phase introduced by DM is represented as:

$$\phi_c = \Sigma_{i=1}^N c_i r_i(u). \tag{1-3}$$

Where N is the number of actuators, c_i the coefficient and $r_i(u_i)$ the response function of each actuator with input voltage u_i.

The goal of this project can be formulated as: to identify a set of response functions r_i, with a series of PSFs as output measurement and control voltage u_i as input.

Chapter 2

Previous Work

In this chapter, the basic theory about light propagation and image formation used in this thesis is introduced, along with a brief introduction to Adaptive Optics (AO) systems. Then, the problem of Deformable Mirror (DM) characterization is stated, which pointed to the topic of wavefront sensing. Wavefront sensing methods used in Wavefront sensorless (WFSless) settings and phase retrieval problem are introduced at last, followed by a summary on relevant works of DM characterization.

2-1 Basics of Adaptive Optics

2-1-1 Light Propagation and Image Formation

In physical optics, monochromatic light wave is represented by a complex function:

$$W(\mathbf{x}, t) = A(\mathbf{x})\text{Re}[e^{i(\omega t - \phi(\mathbf{x}))}] = \text{Re}[A(\mathbf{x})e^{-i\phi(\mathbf{x})}e^{i\omega t}] = \text{Re}[a(\mathbf{x})e^{i\omega t}]. \tag{2-1}$$

where $\mathbf{x} = (x, y)$ is the spatial coordinate, $A(\mathbf{x})$ the amplitude, $a(\mathbf{x}) \triangleq A(\mathbf{x})e^{-i\phi(\mathbf{x})}$ the complex amplitude, $\omega t - \phi(\mathbf{x})$ the phase, the angular frequency $\omega = \frac{2\pi c}{\lambda}$ where c the speed of light and λ the wavelength of this light.
When ω is determined, that is, for the monochromatic case, the time-dependent component can be left out and the light can be fully determined by the complex amplitude:

$$a(\mathbf{x}) = A(\mathbf{x})e^{-i\phi(\mathbf{x})}. \tag{2-2}$$

A wavefront is defined as a surface with equal phase, that is:

$$\omega t - \phi(\mathbf{x}) = \text{const.}, \tag{2-3}$$

and the distribution of optical phase in a plane $\phi(\mathbf{x})$ can very often approximate the whole wavefront $w(\mathbf{x})$ Ref[7], that is:
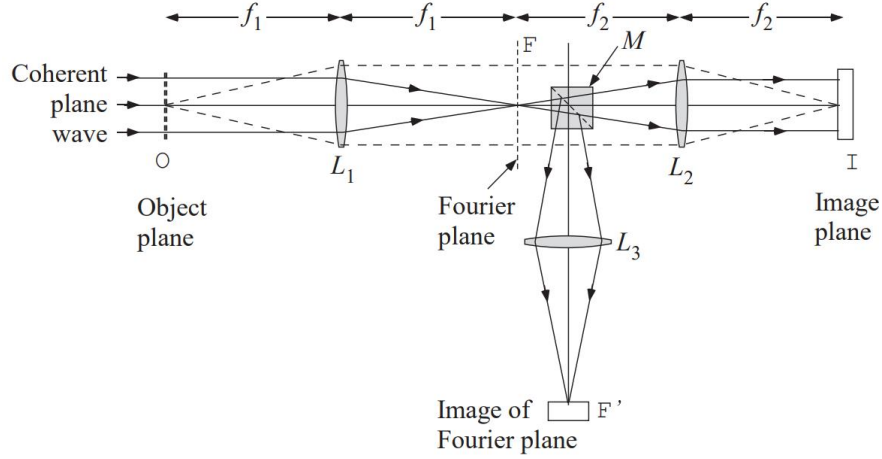
$$w(\mathbf{x}) \approx \phi(\mathbf{x}). \tag{2-4}$$

Figure 2-1: Optical imaging system to illustrate the Abbe theory of image formation. The beam-splitter *M* and lens L_3 are used to form a separate image of the Fourier plane. Source: Ref[8]

Lens is a fundamental element in an optical system and can be viewed as a Fourier transformer Ref[7]. In paraxial approximation the phase delay introduced by a lens with focal length f is represented as:

$$\Delta\phi(\mathbf{x}) = e^{\frac{ik}{2f}(x^2+y^2)}. \tag{2-5}$$

Using $W_0(\mathbf{x}) = Ae^{-i\phi(\mathbf{x})}$ with amplitude A and aberration $\phi(\mathbf{x})$ to represent an incident plane wave, $P(\mathbf{x})$ to represent the pupil function, the resulting wave is proportional to the Fourier transform of the $W_0(\mathbf{x})$ multiplied by $P(\mathbf{x})$ and phase term $e^{\frac{ik}{2f}(u^2+v^2)}$. That is, the wave after a lens is represented as:

$$W(u,v) = \frac{e^{\frac{ik}{2f}(u^2+v^2)}}{i\lambda f} \iint_{\mathbb{R}^2} W_0(\mathbf{x})P(\mathbf{x})e^{-i\frac{2\pi}{\lambda f}(xu+yv)}dx. \tag{2-6}$$

Under diffraction theory of image formation, an optical image can be represented as the Fourier transform of the Fourier transform of the object with phase delays Ref[8], as the image formation is considered as a double process of diffraction and the Fraunhofer diffraction pattern amplitude is described by the two-dimensional Fourier transform of the mask transmission function under Abbe sine condition. As shown in Figure2-1, illumination observed in the focal plane is the Fraunhofer diffraction pattern of the object and the image is the Fourier transform of this diffraction pattern.

The image is the intensity part of the Fourier transform:

$$I(u,v) = \frac{A^2}{\lambda^2 f^2}|\iint_{\mathbb{R}^2} P(\mathbf{x})e^{-i\frac{2\pi}{\lambda f}(xu+yv)}dx|^2. \tag{2-7}$$

Notice that the image only records the intensity and the phase is lost. To reconstruct a complex field, the phase has to be determined. This is called the phase problem and is closely related to the topic of this project and will be treated in the later parts of this chapter.

The far field diffraction pattern of a point source is called the Point Spread Function (PSF). In an ideal telescope such pattern is described by an Airy disc:

$$p_0(\alpha) = \frac{\pi D^2}{4\lambda^2}\left(\frac{2J_1(\pi D|\alpha|/\lambda)}{\pi D|\alpha|/\lambda}\right)^2. \tag{2-8}$$

where α is the angular coordinate, D the diameter of the aperture, J_1 the Bessel function of the first kind.

Extended object can be considered as a collection of point sources and each source produces such PSF. The final image is the intensity of all the PSFs added, making it the convolution of the object intensity and PSF.

$$i = p * o. \tag{2-9}$$

The image of a point source, such as laser source, is the convolution of its PSF and a δ-function, making the image equivalent to the PSF itself.

Resolution describes an imaging system's ability of distinguishing between two point sources. If the central maximal of intensity of one PSF pattern lies outside the first minimum of the other, the two point sources are considered distinguishable according to Rayleigh's resolution criterion. Rayleigh's criterion is represented as:

$$\theta = \frac{1.22\lambda}{D}. \tag{2-10}$$

which is inherited from equation(2-8), as the radius of the first dark ring in the Airy pattern. θ is called the minimal angular separation of two point sources. Equation(2-8), equation(2-9) and equation(2-10) indicate that the image is a smoothed version of the object and aperture size is responsible for the degradation of the image quality since PSF is determined by aperture size. Such resolution degradation is called diffraction limited. We cannot get rid of diffractive effects, the best we can do is to reach this diffraction limit Ref[9].

2-1-2 Adaptive Optics (AO) System and Compensation

Wavefront aberrations are the principle cause of degradation of image quality. Phase conjugation is the most common approach to correct for aberrations and is the basis for most forms of adaptive optics Ref[9]. As is shown in Figure2-2, if a plane wave is distorted, there might be a way to alter the mirror or lens such that the second passage has no distortion. Such alteration in essence multiply the field if the plane wave $|E|e^{-i\phi}$ by its complex conjugate $e^{+i\phi}$, thus the name phase conjugation Ref[9].

Based on the idea of phase conjugation, many AO systems have been designed. Assuming an incoming plane wave from a certain light source, change in optical path changes the phase of the wave. AO system tries to cancel out such distortions by actively introducing optical path length differences on the deformable mirror.

Typical functions of an AO system include basic optical beam propagating, wavefront sensing, phase changing and imaging. Wavefront sensing can be done with or without a WF sensor, such systems are referred to as Wavefront sensor (WFS) and Wavefront sensorless (WFSless) AO systems respectively. DM is considered as the actuator and a crucial part of the system and will be discussed in more detail in the following section.
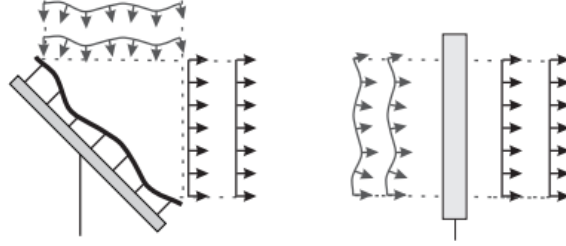
Figure 2-2: Illustration of phase conjugation principle. Wavefront correction with deformable mirror(left) and liquid-crystal phase modulator(right). Source: Ref[7]

2-2   Problem of Deformable Mirror (DM) Characterization

Deformable mirror performs a crucial role in controlling the wavefront. This section aims to provide a general mathematical description of DM and use this to illustrate the characterization problem.

2-2-1   Modeling Characterization of Deformable Mirror (DM)

Membrane DMs have many actuators, their response can be described by influence functions. Theoretical forward modeling of influence function needs to consider physical parameters including thickness, modulus of elasticity and Poisson's ratio Ref[10][9].

Assuming each actuator to be independent and linear sum of influence functions represent the mirror surface, given a set of actuator signals $\mathbf{u_m} \in \mathbb{R}^N$, , N is the number of actuators of the DM. The corresponding mirror deformation ϕ_c can be represented as:

$$\phi_c = A_m \mathbf{u_m}, \tag{2-11}$$

where A_m is the influence matrix of the mirror, $A_m \in \mathbb{R}^{M \times M \times N}$ where M is the size of the phase map. It can be used to generate a desired target wavefront ϕ_0 by pseudo inverse using singular value decomposition (SVD) Ref[11]:

$$A_m = USV^T, \tag{2-12}$$

$$A_m^{-1} = VS^{-1}U^T, \tag{2-13}$$

the interpretation of each matrix in SVD is as follows, columns of U is a set of N spatial modes of the mirror, diagonal elements of S are the gain of the modes, columns of V is an orthogonal set of actuator signals. The smaller the gain the larger input signal is needed to produce a same amount of the mode Ref[11].

Thus given a desired wavefront ϕ_0, the control signal can be determined and the produced wavefront can be represented:

$$\mathbf{u_m} = f(VS^{-1}U^T \phi_0), \tag{2-14}$$

$$\phi_c = USV^T f(VS^{-1}U^T \phi_0), \tag{2-15}$$

where $f(\cdot)$ is a clipping function used to represent the limited stroke of the mirror actuators:

$$
f = \left\{ \begin{array}{ll} x_i & \text{for} \quad |x_i| \leq x_{max}, \\ x_{max} \frac{x_i}{|x_i|} & \text{for} \quad |x_i| \geq x_{max}. \end{array} \right.
$$

once the influence matrix and its inverse are known, the DM is characterized. Current methods for characterization of an DM are discussed in chapter 3.

On the other side of the equation(2-11), ϕ_c is used to represent the wavefront generated by the DM. Instead of driving the individual actuators directly, the usual approach is to use a modal basis like Zernike polynomials, which can be generated by a certain combination of control signals Ref[12]:

$$
\phi_c(r, \theta) = \sum_{i=1}^{\infty} a_i Z_i(r, \theta), \tag{2-16}
$$

where a_i is the amplitude of Zernike mode $Z_i(r, \theta)$. r, θ are the radius and angle used in polar coordinates. Stacking the coefficients of Zernike polynomials to a vector $\mathbf{a}$ can be another way to decompose the desired wavefront:

$$
\mathbf{a} = B\mathbf{u_m}. \tag{2-17}
$$

2-2-2   Wavefront Sensing

Wavefront sensing is the process of identifying the incoming wavefront to an AO system. Sensor-based wavefront sensing uses setups like interferometers, curvature sensors, and Shack-Hartmann sensors. In contrast, sensorless or "phase retrieval" wavefront sensing, which is the focus of this project, does not rely on specific sensors. This thesis aims to solve DM characterization problem in sensorless settings.

Phase Retrieval Problem

Following the image formation discussed in previous sections, phase retrieval problem can be formulated. Supposing a monochromatic light field W in the pupil plane with amplitude A, and unknown phase ϕ:

$$
W = Ae^{-i\phi},
$$

the intensity image I in the focal plane can be represented as:

$$
I = |\mathcal{F}(W)|^2 * \delta = |\mathcal{F}(W)|^2.
$$

I is also the PSF for the point source case. The phase retrieval problem is to determine phase given the intensity measurement and knowledge of Fourier transform.

Phase retrieval problem can be more abstractly formulated as in Ref[13]:

$$\text{Given function: } a : \mathbb{R}^2 \to \mathbb{R}_+$$
$$b : \mathbb{R}^2 \to \mathbb{R}_+$$
$$\text{Find function: } W : \mathbb{R}^2 \to \mathbb{C}$$
$$\text{satisfying: } |W| = a \quad \text{and} \quad |\mathcal{F}(W)| = b.$$

here $\mathbb{R}_+$ denotes the non-negative real numbers and the modulus the pointwise Euclidean magnitude.

This problem is to find the phase of a complex-valued function, given its pointwise amplitude and pointwise amplitude of its Fourier transform.

Phase Retrieval Methods

There are 3 major kinds of phase retrieval algorithms, i.e., alternating projection (AP), semidefinite programming (SDP) and transport-of-intensity equation (TIE) Ref[6], while recent developments including use of differential optical transfer function (dOTF) and deep learning. Due to the large amount of appliance and variations, AP methods would be discussed in details.

Gerchberg and Saxton proposed a simple and practical method for determining phase, by iteratively imposing constraints on real and Fourier plane Ref[14]. Fienup generalized the Gerchberg-Saxton (GS) algorithm showing that the directions of projections are formally similar to directions of steepest descent for a squared set distance metric Ref[15], and GS-like methods are later viewed as a projection-type algorithm involves non-convex sets Ref[16]. Such methods take iterative steps, raising discussing on the convergence guarantee Ref[16] and initialization Ref[17].

The original Gerchberg-Saxton algorithm takes iterative Fourier transformation back and forth between the object and Fourier domains. In each iteration, the algorithm consists of 4 basic steps.

First, denoting the estimate of the field in the image plane at step k as $g_k(x)$, where x denotes the image plane coordinates. Taking it's Fourier transform yields:

$$G_k(u) = \sqrt{|G_k(u)|}e^{i\phi_k(u)} = \mathcal{F}[g_k(x)], \tag{2-18}$$

where u is the pupil plane coordinate and $G_k(u)$ is the Fourier transform of the image plane field and thus denotes the field in the pupil plane.

Second, for the field $G_k(u)$ in the pupil plane, we replace its estimated amplitude with the ground truth amplitude $|F(u)|$, which is the pupil function of the optical system:

$$G'_k(u) = \sqrt{|F(u)|}e^{i\phi_k(u)}. \tag{2-19}$$

This amplitude replacement can be viewed as imposing constraint during projection from image plane to pupil plane.

Third, inverse Fourier transform the pupil plane field result in the updated image plane field $g'_k(x)$:

$$g'_k(x) = \sqrt{|g'_k(x)|}e^{i\theta'_k(x)} = \mathcal{F}^{-1}[G_k(u)]. \tag{2-20}$$

Lastly, replace the amplitude with that of the measured image amplitude $|f(x)|$ to get an updated estimate of the image:

$$g_{k+1}(x) = \sqrt{|f(x)|}e^{i\theta_{k+1}(x)} = \sqrt{|f(x)|}e^{i\theta'_k(x)}. \tag{2-21}$$

Equation(2-18) to equation(2-21) are the iteration steps for the Gerchberg-Saxton algorithm. A list of symbols are summarized in table2-1.

Notation	Meaning
x	Image plane coordinates
u	Pupil plane coordinates
$g_k(x)$	Complex field in the image plane
$G_k(u)$	Complex field in the pupil plane
$F(u)$	Ground truth pupil function of the optical system
$|F(u)|$	Amplitude in the focal plane, usually an aperture function.
$f(x)$	Ground truth field in the image plane
$|f(x)|$	Intensity measurement in the image plane.

Table 2-1: Notations used for Gerchberg-Saxton (GS) algorithm

Such algorithms can be generalized to any problem where partial constraints are known in each of two domains, in this case image and Fourier domains.

2-3   Previous Works on Sensorless DM Characterization

Previous work on DM characterization mainly focuses on the use of various sensors, such as interferometers, Shack-Hartmann Wavefront Sensor (SHWFS), and even wavefront generators as discussed in Ref[12, 18, 3, 19, 20, 21]. The advantages of using wavefront sensors include the accuracy of calibration results and smaller processing time, while their drawbacks include the extra hardware and alignment needed, as well as accuracy limited by reconstruction modes.

This thesis focuses on the characterization of DM in WFSless setups. Relative works in this setting is much less than in WFS-based settings. There nevertheless still exists several works including Ref[22, 23, 24, 25, 26, 5, 27, 28]. Majority of the characterization works took the model-based path, which exploiting the theoretical model of the DM or the second moment of intensity measurement, while some focused on using phase diversity methods.

2-3-1 Model-based DM Characterization

In Ref[22] a model-based data-driven method for DM calibration is proposed, where the AO system is first modeled based on the intensity measurements and then identified for aberrations using SDP, the control law is obtained by solving an optimization problem.

In Ref[26]. a calibration scheme using optimal modes which are insensitive to misalignments and the shape of illumination profile is proposed. However this work assumes known response functions and decompose it to form "optimal modes" for better control performance. This work does not focus on the acquisition of response functions but does give an example for how to refine the approximate control laws.

In Ref[5], a model-based DM calibration method is proposed. The model makes use of a linear relationship between mean square of aberration gradients and the second moment of the image intensity distribution. But still, this work assumes a known theoretical response functions of DM.

It can be seen that model-based methods for DM calibration in sensorless settings are usually more focused on the refined tuning of response functions instead of acquisition of such response functions. However, this thesis aims to obtain a series of response functions in the first place.

2-3-2 Phase Diversity Based DM Characterization

In Ref[25], a modal based DM calibration process for WFSless AO system is proposed. An approximately characterized mapping between input voltage and Zernike coefficients is first obtained. Denote such control matrix as $\mathbf{A_m}$, input voltage as $\mathbf{u_m}$ and wavefront coefficients as α which are determined by phase diversity methods. The acquisition of control matrix is based on the following:

$$\mathbf{u_m} = \mathbf{A_m}\alpha, \tag{2-22}$$

$$\mathbf{A_m} = \mathrm{pinv}(\mathbf{E}^+), \tag{2-23}$$

$$\mathbf{E}^+{}_{i,j} = \frac{\partial \alpha_i}{\partial u_{mj}}. \tag{2-24}$$

where $\mathbf{A_m}$ can be represented as a pseudo-inverse of a matrix $\mathbf{E}^+$, and thus $\alpha = \mathbf{E}^+ \mathbf{u_m}$. $\mathbf{E}^+$ in equation(2-24) denotes the mirror's wavefront response to input voltages, where α_i is the wavefront coefficient determined by Phase Diversity (PD). Thus the control matrix is measured.
After this, the control matrix is further calibrated in a closed-loop. The results of the control matrix measurement is used to generate flat wavefronts. Strehl Ratio (SR) and wavefront Rooted Mean Square (RMS) are used as quality measurement for the calibration loop.

In Ref[23], a more straight forward method is proposed. In this work, phase diversity is introduced by a piezo stage moving back and forth to create axial displacement. After this, Phase Diversity Phase Retrieval is used to retrieve phase for each actuator's steps. However, this method also uses an extra hardware of piezo stage, which is convenient for lab microscopes but not ideal if DM alone needs to be calibrated.

2-4 Conclusion

In this chapter, basics of AO and DM calibration is introduced and relative work on DM characterization is also discussed.

It can be seen that the characterization of DM using WFSless method is possible but there is not so many work on this topic. Current studies mainly focus on the fine-tuning of existing response function and implicitly assumes a known theoretical response function. Only limited number of works focuses on the acquisition of original response function and majority of them uses phase diversity based methods.In these researches, phase diversity is usually introduced by additional hardware such as piezo motors or beam splitters.

This chapter intends to present basic knowledge of AO and current status of relevant research. Based on this, a characterization scheme would be proposed in the next chapter.

Chapter 3

Calibration Scheme

In this chapter, issues of DM calibration are discussed, including the setup available for the experiment, methods of generating diversity phase and the proposed method of characterizing the DM.

3-1 Considerations of DM Characterization

3-1-1 DM Characterization Using DM Generated Diversity

As discussed in the previous chapter, the characterization of DM in WFSless settings is possible in principle. Results of literature review indicates that there are now 2 mainstream paths of doing this, one is through model-based methods which assumes theoretical response functions available, the other is through phase diversity phase retrieval to obtain response function from measurement.

Characterization of a DM is to determine its response functions purely from measurement. Such characterization is useful when the theoretical model of a DM is not available or there are large discrepancies between actual and theoretical response functions. This thesis aims to characterize the DM, obtaining the response functions even when the theoretical models are not available.

Since response function in essence is a mapping between input voltage and DM shape, it might seem that performing phase retrieval to intensity measurement of all input signals would be enough. However, as will be shown in later chapters, primitive phase retrieval method of Gerchberg-Saxton will not be sufficient due to issues including twin phase and spinning phase. This is also part of the reasons why most works adapt phase diversity methods.

To introduce a phase diversity in an optical system, a common way is using extra hardware to change the optical light path and take multiple intensity measurement for phase retrieval algorithm.

However, it is often not noticed that the DM itself can introduce a phase diversity. If we can use the diversity generated by the DM itself to run the characterization, the whole process would be largely simplified. This would then be the idea of this thesis, i.e., based on the phase diversity path of characterization, using DM generated phase diversity to characterize the DM.

To validate this idea, a set of simulations and experiments are designed and will be treated in the following chapters. In the next section, hardware setup available in the laboratory will be introduced, after this the phase retrieval method to be used in this project would be discussed. The characterization scheme for the DM would be introduced at last.

3-1-2 The setup available

To characterize a DM, a set of basic AO system is enough. A setup is used for this thesis is shown in Figure3-1.

(a) Initial setup available.   **(b)** Scheme of initial setup.
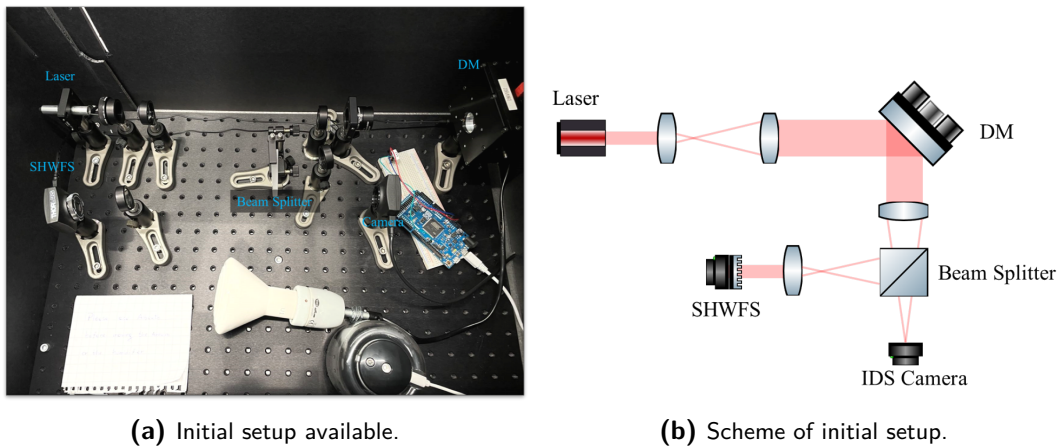
Figure 3-1: Initial setup available in the lab.

In this setup, there are 4 lenses of 20cm focus. The laser is of 632nm wavelength. The DM used is a 96-channel membrane mirror from Flexible Optics.B.V. Ref[29], as shown in Figure3-2. The camera is an 8-bit mono color IDS UI-154xLE-M Ref[30] with 1280×1024 pixels and pixel size of 5.6nm. Apart from this, a SHWFS is on the other arm of the beamspliter, this SHWFS is used by another person. Detailed parameters of the setup would be given later in section4-1.
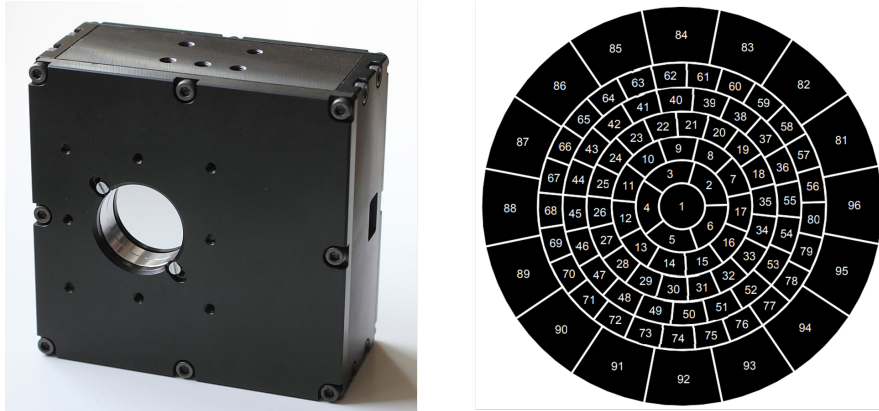
Figure 3-2: The Deformable Mirror used in this project and its layout.

To test the imaging quality of this setup, a PSF is taken after an optimization program is complete. This program uses Nelder-Mead algorithm to optimize image metric of multiplication of distance of each pixel to center of gravity and pixel value. After 3000 iterations the PSF is as shown in Figure3-3a.


(a) PSF of initial setup.
The size of the PSF is approximately 10 pixels across.

(b) PSF of modified setup.
The size of the PSF is approximately 100 pixels across.
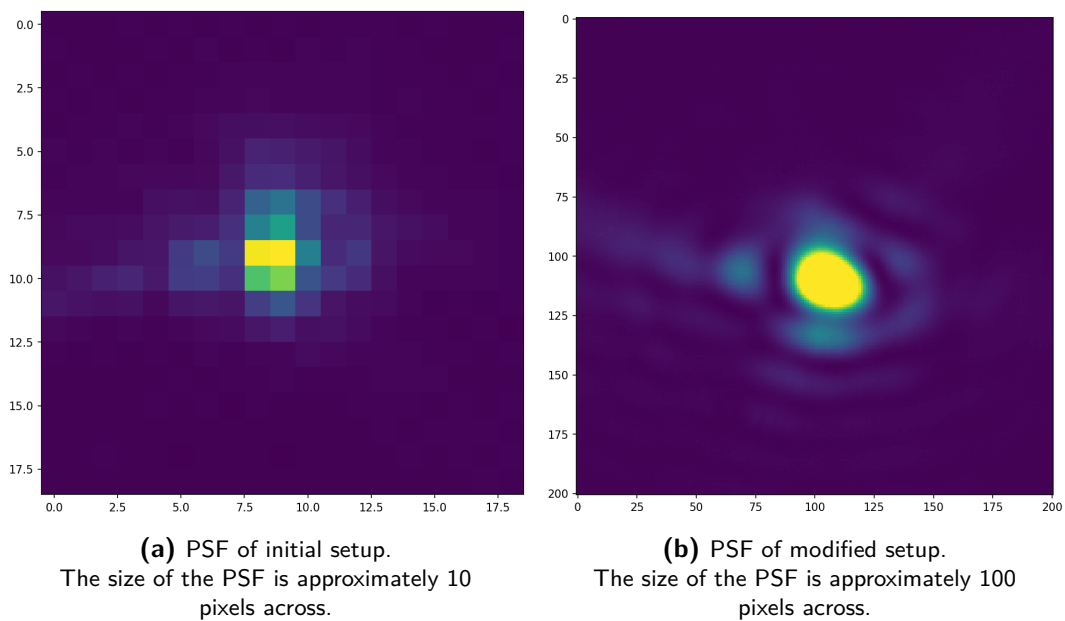
Figure 3-3: PSF of setup before and after modification. After the modification the size of the PSF is 10 times larger. Both figures are captured on the camera of 1280×1024 pixels, cropped to central part of 20 and 200 pixels respectively. PSF on the right has more details and allows for finer phase retrieval results.

It can be seen that this PSF is small in size, with merely ~ 10 pixels across in the central part. This size is close to the size from theoretical calculation but still too small for image-based characterization. Also some stray light is observed in the area far from center, this indicates that the setup needs to be modified and re-aligned. This is because alternative projection phase retrieval methods are heavily dependent on the intensity measurement used, artifacts

in the PSF may cause phase retrieval being non-converging and invalid.

To enlarge the visible PSF area, an microscope objective of $10\times$ is added between beam splitter and camera, as is shown in Figure3-4. The resulting PSF is shown in Figure3-3b, it can be seen that the diameter of the pattern increased 10 times and the PSF pattern is now large and clear.
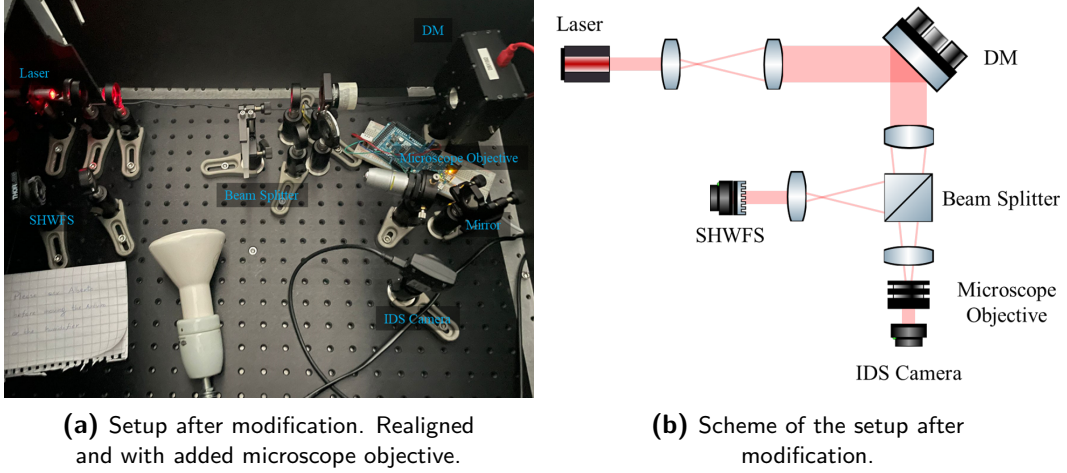

(a) Setup after modification. Realigned and with added microscope objective.

(b) Scheme of the setup after modification.

Figure 3-4: Setup after modification. A microscope objective of $10\times$ is added in front of the camera, resulting in a $10\times$ larger PSF.

The setup shown in Figure3-4b is now suitable for characterizing the DM, as it has all the essential part of an AO system, as well as a SHWFS which is initially used by another person but can still be used for validation of results.

3-1-3   Generating Diversity Phase

As discussed before, using DM to generate a diversity phase would largely simplify the DM characterization process. This subsection discusses the possible ways of generating and calibrating a diversity phase using the DM, i.e., how to use the un-calibrated DM to produce a known and stable diversity phase. To obtain a calibrated phase diversity, two methods have been tried.

Diversity phase generation using unified input

Denote a unified input signal $\mathbf{u}_d$ as:

$$\mathbf{u}_d(p,q) = [\; \underbrace{p,...,p}_{q \text{ inputs with value } p} \;,\; \underbrace{0,...,0}_{N-q \text{ inputs with value } 0} \;].$$

This signal gives a same value p for the first q actuators and 0 input for all other actuators.

The first is a straightforward methods, as long as a constant input signal is sent to the DM, the DM would generate a same phase. Based on this and superposition principle, a diversity

phase can be obtained by subtracting two different phase, it's corresponding input signal is also obtained by subtracting two different input signals.

Denote the intensity measurement of input signal $\mathbf{u}_1$ as I_1, the corresponding phase at this time is ϕ_1. Using GS algorithm ϕ_1 can be retrieved:

$$\phi_1 = \texttt{GS}(I_1). \tag{3-1}$$

For another input signal $\mathbf{u}_2 = \mathbf{u}_1 + \mathbf{u}_d$, denote its intensity measurement as I_2 and corresponding phase ϕ_2, we have:

$$\phi_2 = \texttt{GS}(I_2). \tag{3-2}$$

We can establish a link between input signal $\mathbf{u}_d$ and diversity phase ϕ_d as:

$$\phi_d = \phi_2 - \phi_1, \tag{3-3}$$
$$\mathbf{u}_d = \mathbf{u}_2 - \mathbf{u}_1. \tag{3-4}$$

Hence a link between DM signal and DM shape $(\phi_d, \mathbf{u}_d)$ has been established. Use this phase-DM signal relation, phase diversity phase retrieval can be performed in anytime during characterization.

Diversity phase generation based on PSF Optimization

The other method is to generate a defocus phase via optimizing PSF. Considering defocus is one of the most used diversity in PDPR, also considering that the DM is mounted in a bowl-shape manner, which corresponds to defocus when no input voltage is given, it would be sensible to have DM generate a defocus phase as diversity phase.

Denote the analytical phase of defocus as $\phi_{defocus}$, use forward model to simulate the PSF the setup would produce and denote it as I_{sim}:

$$I_{sim} = \texttt{Simulation}(\phi_{defocus}). \tag{3-5}$$

For an input signal $\mathbf{u}$, denote the PSF measurement of the setup as a function of input signals: $I_{measure}(\mathbf{u})$. Use input signal as manipulating variables and error between simulated and measured PSF as cost function, we can get a input signal $\hat{\mathbf{u}}$:

$$\hat{\mathbf{u}}_d = \arg\min_{\mathbf{u}} |I_{sim} - I_{measure}(\mathbf{u})|. \tag{3-6}$$

This input signal $\hat{\mathbf{u}}_d$ is a signal that make the DM produce a shape that generates a PSF as close to I_{sim} as possible.

Denote the phase of the setup as ϕ_d, which is retrieved by GS:

$$\phi_d = \texttt{GS}(I_{measure}(\hat{\mathbf{u}}_d)). \tag{3-7}$$

Ideally $\phi_d \approx \phi_{defocus}$, thus we can use $\phi_{defocus}$ as initial guess for the GS. The idea behind this is that when the 2 PSFs are close enough, the phase from the setup would be close to the analytical defocus phase.

$$I_{measure}(\hat{\mathbf{u}}_d) \rightarrow I_{sim}, \tag{3-8}$$

$$\phi_d \rightarrow \phi_{defocus}. \tag{3-9}$$

Of course this is not always true since there is no one-to-one correspondence between phase and intensity. But use this as an prior information and setting the initial guess of GS to be $\phi_{defocus}$, there is a large chance that the GS converge to a correct phase quickly.

In conclusion, both methods can be used to obtain diversity phase. The latter method presumably would be more accurate than the first one, as starting point of GS can be set to the defocus phase, and this starting point would be very close to the real phase. However in the first method the DM could end up in a totally unknown state and multiple starting point might need to be tried. A drawback of the latter method would be the extra time needed for the PSF optimization.

3-2   The Proposed DM Characterization Scheme

Using Phase Diversity Phase Retrieval to characterize the DM, the process can be straightforward, as shown in Figure3-5.
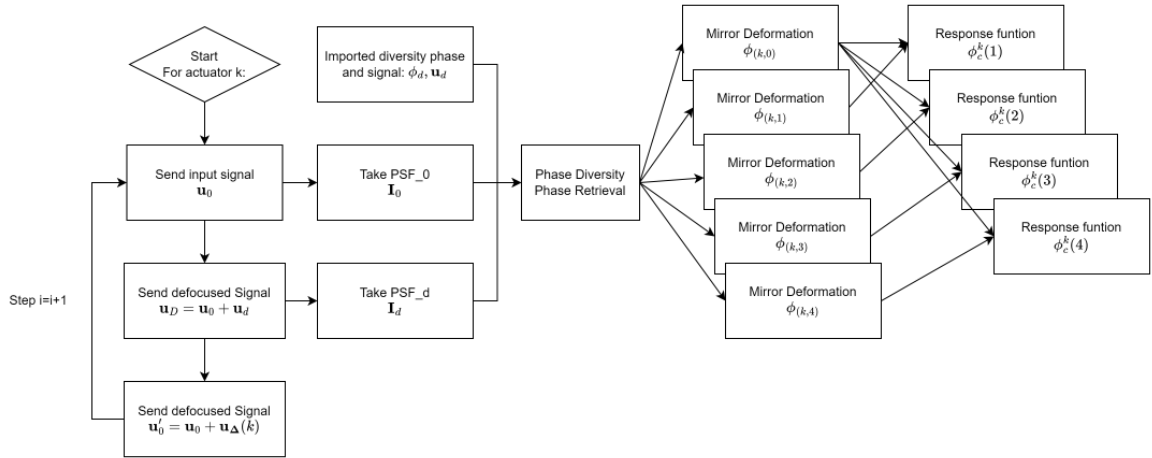

Figure 3-5: Simulated Deformable Mirror Calibration Process. PDPR is used for each actuator's each input change. For each PDPR round, zero initial input signal $\mathbf{u}_0$, imported diversity phase ϕ_d and imported diversity signal $\hat{\mathbf{u}}_d$ or $\mathbf{u}_d$ are used. To update the input signal, $\mathbf{u}_\Delta(k)$ as described in equation(3-10) is used. For actuator k, input step i, step response $\phi_c(k)^i$ is obtained by subtracting 2 retrieved phase maps as $\phi_c(k)^i = \frac{\phi_{(k,i)} - \phi_{(k,0)}}{i}$.

In this approach, phase retrieval methods are used to determine wavefront phase, which is then used to map between actuator input and DM response. The phase retrieval method could vary and PDPR-GS algorithm is taken for example at present and would be discussed in the next chapter.

Initialization This step aims to make the DM as flat as possible, so that the first GS iteration can start with a flat phase map as initial position.

1. Use Nelder-Mead and the metric function to flatten the DM.
2. Store the corresponding DM input as $\mathbf{u}_0 \in \mathbb{R}^{96}$

Actuator Calibration This step aims to create a mapping between input voltage and resulting phase. This step is repeated for each actuator.

1. Send $\mathbf{u}_0$ to make the DM flat.
2. For actuator $k(1 \le k \le 96)$:

   (a) For step $i(1 \le i \le M)$, where M is the step number of choice:

       i. Update input signal:

   $$\mathbf{u}_0' = \mathbf{u}_0 + \mathbf{u}_\Delta(k), \qquad (3\text{-}10)$$

       where $\mathbf{u}_{(k,i)}$ denotes the input signal of i-th step when characterizing k-th actuator. $\mathbf{u}_\Delta(k) \in \mathbb{R}^{96 \times 1}$ denotes the step-wise change in input signal, it is a vector of all zeros except for the k-th element of 0.1, the step size of choice.

       ii. Send the input signal $\mathbf{u}_{(k,i)}$ and take the PSF measurement I_0.

       iii. Send the diversity signal $\mathbf{u}_D = \mathbf{u}_{(k,i)} + \hat{\mathbf{u}}_d$ and take the PSF measurement I_d, where $\mathbf{u}_d$ is the input signal corresponding to diversity phase ϕ_d as introduced in section3-1-3.

       iv. Run the PDPR algorithm for phase retrieval:

   $$\phi_{(k,i)} = \mathtt{PDPR}(I, I_d, \phi_d). \qquad (3\text{-}11)$$

   (b) Obtain response functions for actuator k:

   $$\phi_c^k(i) = \frac{\phi_{(k,i)} - \phi_{(k,0)}}{i}. \qquad (3\text{-}12)$$

DM Calibration Repeat actuator calibration process for each actuator to calibrate the whole DM.

1. A total of $96 \times M$ mappings between input voltage and resulting wavefront would be created, i.e., for all 96 actuators, M mappings are created for each actuator.
2. Under the assumption for equation(2-11) that the DM has a linear input-output model, M phase maps can be averaged and only 1 mapping for each actuator, thus only 96 response functions should be obtained.

3-3   Conclusion

In this chapter, based on the literature review results, a primitive scheme for characterizing the DM and two methods for obtaining the calibrated diversity phase has been proposed. In the next chapter, simulation models and phase retrieval algorithms based on these schemes would be constructed.

Chapter 4

Numerical Simulation

In this chapter, numerical counterparts of the proposed calibration scheme is implemented, including the forward model of the setup and alternative-projection based phase retrieval methods. A simulated DM characterization using theoretical response functions is also implemented and simulation results could reach a RMSE around 0.02 for most of the actuators.

4-1 Forward Modeling of the Setup

The forward model is a realistic simulation of PSF registering process. The setup used for this project is shown in Figure3-4b. The PSF registered is formed with a 17mm lens with focal length of 200mm, at 632nm wavelength, with IDS UI-1540 camera. The camera quantizes the PSF with 8-bits or 256 gray scales resolution. It's of 1280×1024 pixels large and the pixel pitch is 5.2μm. Some of the key parameters of the setup is summarized in table4-1.

Notation	Meaning	Value
λ	Wavelength	0.632e-6m
f	Focal length	0.20m
D	Aperture diameter	0.017m
Δx	Pixel pitch	5.2e-6m

Table 4-1: Parameters in Forward Model

4-1-1 Implementation of Forward Model

The input and output of the forward model are phases and corresponding PSFs. Denote the input phase map as Φ_0, aperture mask of the AO system as Apt, the phase on the pupil plane

can be represented as:

$$\Phi_p = \text{Apt} \cdot \Phi_0,$$

the complex wave field at the aperture is thus:

$$E = \text{Apt} \cdot \exp\left(\Phi_p \cdot 1j\right),$$

the PSF on the image plane can thus be calculated using Fourier transform:

$$\text{PSF} = |\mathcal{F}(E)|^2.$$

The above modeling is in continuous domain. However the PSF registering process uses a digital camera. Aperture mask `Apt` would serve an important role in discretization of the phase maps, as will be shown later in Figure4-2. To determine the aperture mask, a more detailed discussion on sampling is provided below and the final forward model would be given in the last part of this section.

Focal Plane Considerations

Supposing a focused beam with wavelength λ crossing an aperture with diameter D and focal length f, denoting focal plane sampling pitch as T, as shown in Figure4-1:
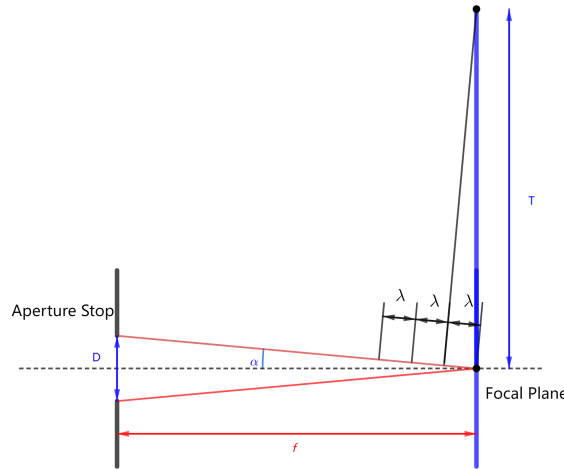

Figure 4-1: Illustration of geometry of aperture and focal plane

according to the geometry, we have:

$$\tan \alpha = \frac{D/2}{f}, \tag{4-1}$$

$$\sin \alpha = \frac{\lambda}{f}. \tag{4-2}$$

Supposing that the angle α is small enough and thus $\tan \alpha \approx \alpha$, and $\sin \alpha \approx \alpha$, we thus have:

$$T = \frac{f\lambda}{D/2}, \tag{4-3}$$

thus the frequency of incoming wave on the focal plane is

$$\nu_{field,img} = \frac{1}{T} = \frac{D}{2f\lambda}. \tag{4-4}$$

This frequency $\nu_{field,img}$ is the maximum frequency of a field in the focal plane one can get from a plane wave behind the aperture.

On the other hand, with Nyquist sampling theorem, the frequency given by the sampling is:

$$\nu_{sample,img} \geq 2\nu_{field,img} = \frac{D}{f\lambda}. \tag{4-5}$$

Pupil Plane Considerations

In the pupil plane, the aperture itself should be sampled to simulate the imaging process. The frequency of wavefield at pupil plane is naturally:

$$\nu_{field,pupil} = \frac{1}{\lambda}, \tag{4-6}$$

while sampling frequency of the pupil is determined by the camera pixel pitch Δx:

$$\nu_{sample,pupil} = \frac{1}{\Delta x}. \tag{4-7}$$

Denote the ratio of pupil and image plane sampling frequency as Q, we have:

$$Q = \frac{\nu_{sample,pupil}}{\nu_{sample,img}} \geq \frac{\frac{1}{\Delta x}}{\frac{D}{f\lambda}} = \frac{f\lambda}{D\Delta x}. \tag{4-8}$$

Ratio Q defines the relative size of the aperture in the discrete representation used as input for discrete Fourier transform to calculate the PSF, as will be shown in the next subsection. It can be seen that this ratio is only dependent on D, f, λ and pupil plane sampling, i.e., $Q(D, f, \lambda, \Delta x)$. That is to say, for a given optical system, with wavelength, focal length, aperture diameter all known, Q is only dependent on pupil plane sampling pitch.

Aperture Mask Considerations

In the forward model, given a aperture picture of certain pixels, it's necessary to determine how larger should the aperture take in this picture so as to keep in line with the real setup. Supposing the PSF and aperture mask picture are both of $M \times M$ pixels, the focal plane sampling frequency of this configuration is thus $1/M$. Denoting the number of pixels of aperture diameter in this picture as N, the spatial frequency is thus $1/N$. Following the modeling in Ref[31], we have:

$$Q = \frac{1/N}{1/M} = \frac{M}{N}. \tag{4-9}$$

The Forward Model

Having considered the above issues, the forward modeling in discrete domain can be derived. Given a phase map Φ_0 of size $L \times L$ pixels, the corresponding aperture function is determined by Q value as described in equation(4-9). The radius of the aperture mask would be:

$$R_{apt} = \frac{L}{2Q}. \tag{4-10}$$

The aperture mask can then be constructed as:

$$\mathtt{Apt} = \mathtt{np.zeros([L,L])},$$
$$\mathtt{Apt}[x^2 + y^2 < R_{apt}] = 1,$$
$$\mathtt{Apt}[x^2 + y^2 > R_{apt}] = 0.$$

An example of aperture mask of size 201×201 with different Q values are shown in Figure4-2.
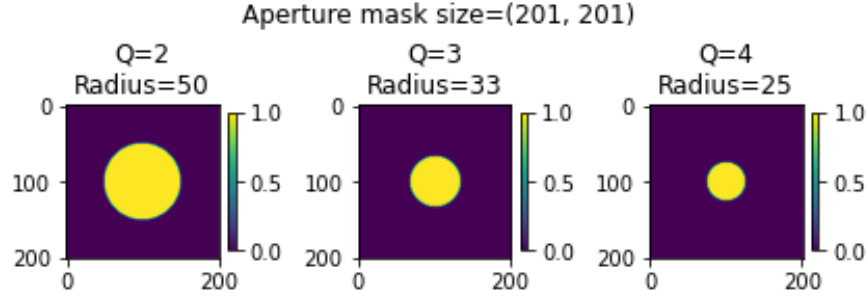

Figure 4-2: Aperture mask of size 201×201, with different Q values. This example is used to show how would choice of Q influence the aperture and forward model configuration.

The simulated PSF is thus:

$$I_{sim} = |\mathtt{FFT}(\mathtt{Apt} * \exp{(\mathtt{Apt} * \Phi_0 * 1j)})|^2$$

where the aperture function $\mathtt{Apt}$ is a function of Q:

$$\mathtt{Apt}(Q),$$

which is a function of several parameters of the setup:

$$Q(D, f, \lambda, \Delta x).$$

Packing all variables together we arrived at a compact description of the forward model

$$I_{sim} = \mathtt{FWsim}(D, f, \lambda, \Delta x, \Phi_0),$$

where:

$$\mathtt{FWsim} := |\mathtt{FFT}(\mathtt{Apt}(D, f, \lambda, \Delta x) * \exp{(\mathtt{Apt}(D, f, \lambda, \Delta x) * \Phi_0 * 1j)})|^2$$
$$= |\mathtt{FFT}(\mathtt{Apt}(Q) \exp{(\mathtt{Apt}(Q) * \Phi_0 * 1j)})|^2.$$

Thus the forward modeling of the AO system without the DM is complete, a Python code of the forward model is given in appendixB-1.

4-1-2   Forward Model Validation

The forward model takes phase map as input and returns PSF of corresponding system as output. To validate the forward model, simply tune the DM on setup to be flat, then compare the registered PSF with the simulated PSF from the forward model.
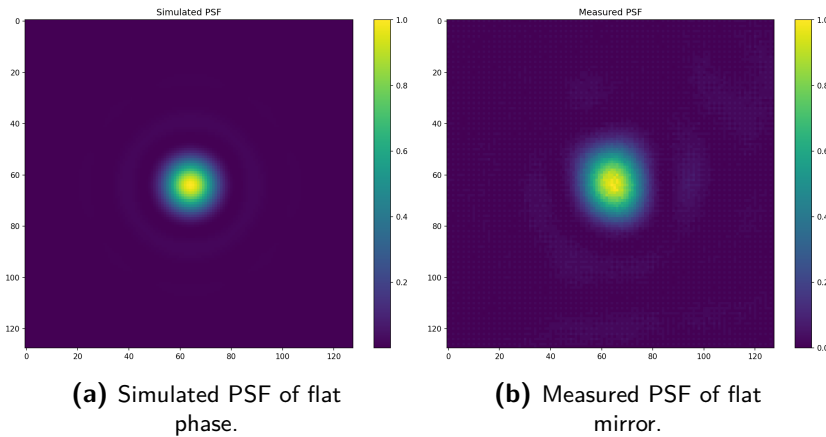

(a) Simulated PSF of flat phase.

(b) Measured PSF of flat mirror.

Figure 4-3: PSFs of flat phase, from simulation model(left) and setup(right). The flat mirror of setup is obtained using BeamTuner software which optimizes the input signals. Two PSFs match with each other and corresponds with the Airy pattern given by equation(2-8), which validates the built forward model.

As is shown in Figure4-3, both PSFs are approximately in the same shape as given by Airy pattern formula described in equation(2-8), the first edge has a radius of ~ 20 pixels. The measured PSF is in a more irregular shape, this is normal since there is always some aberrations cannot be eliminated in the setup either by aligning or optimizing DM. This suggests that the forward modeling of the setup is correct.

4-2   Alternative-Projection Based Phase Retrieval Methods

As discussed in previous sections, alternative-projection based phase retrieval methods such as Gerchberg-Saxton (GS) algorithm are commonly used in the field of AO. In this section, implementation of GS algorithm, as well as GS based PDPR are shown.

4-2-1   Gerchberg-Saxton (GS) Algorithm

As described in section2-2-2, the GS algorithm can be easy as few lines of codes. As shown in Figure4-4, GS basically project the complex field back and forth between image plane(spatial domain) and pupil plane(Fourier domain), while keeping the amplitude the corresponding to the ground truth. When the phase term converge, the phase is retrieved. It's worth noticing that there is no convergence guarantee for this method and even if the phase converges, there is no guarantee that the phase is actually the ground truth phase, since the phase retrieval problem is ill-posed in its nature.
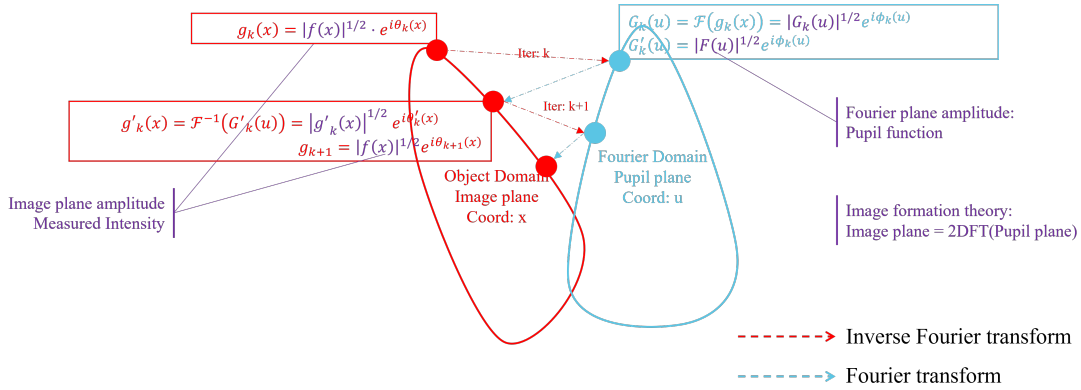
Figure 4-4: Illustration GS process as described in Algorithm1. Notations are followed from table2-1, implementation is listed in AppendixB-2.

An overview of such algorithm shown in Algorithm1 and implementation in Appendix, where x indicates image plane coordinates, u indicates pupil plane coordinates, $g_k(x)$ indicates the complex field in the image plane at k-th iteration, $G_k(u)$ indicates the field in the focal plane field at k-th iteration and $f(x), F(u)$ indicates the intensity distribution in the image and focal plane respectively.

Algorithm 1 Gerchberg-Saxton (GS) Algorithm

Given: measured intensity $|f(x)|$, Fourier plane intensity(aperture mask) $|F(u)|$, initial guess phase `phi_0`

```
p_0 = sqrt(|f(x)|): Square root of intensity measurement.
a = sqrt(|F(u)|): Square root of aperture mask.
g_k(x) = a * exp(phi_0 * 1j): Initial guess of field in the image plane.
```
while `k < max_iter` **do**
   `G_k(u) = fft2d(g_k(x)))`
   `g_k(x) = p_0 * exp(angle(G_k(u))`
   `GS_phase = angle(G_k(x))`
   `g_k(x) = ifft2d(g_k(x))`
end while
Return: `GS_phase`

To test the performance of GS algorithm, a PSF is simulated using forward model and artificial lower order phase. The lower order phase is a combination of several Zernike modes, for example, Zernike mode number 6 and 12:

$$\text{Ground\_truth\_phase} = 0.5 * \text{Z\_mod}[6] + 0.5 * \text{Z\_mod}[12].$$

Simulate the PSF using the forward model described in previous section, choose sampling coefficient $Q = 2$ with 201×201 figure size,:

$$\text{PSF} = \text{FWsim}(\text{figure\_size}=200, Q=2, \text{Ground\_truth\_phase}).$$

No noise is added at this point, as the purpose of this simulation is to check the feasibility of the method in the most ideal case possible. For the initial phases, 10 rounds of random phases would be been tried and the seed with best performance would be chosen, so as to minimize the influence of twin phase and residue phases, as will be discussed later in this section.

The setups for GS are shown in Figure4-5, and results are shown in Figure4-6. After ~ 4500 iterations the retrieved phase converges and RMSE with ground truth phase reaches 0.0815.
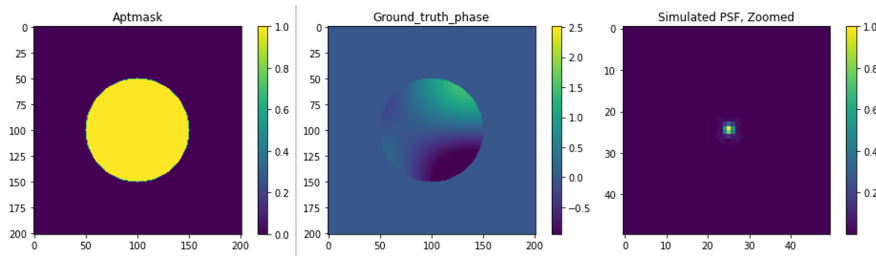

Figure 4-5: Setups for GS testing. Left: Aperture mask of 200×200 pixels with radius of 50 pixels; middle: Analytical ground truth phase; Right: Simulated PSF of ground truth phase, cropped from 200×200 to 50×50 pixels size
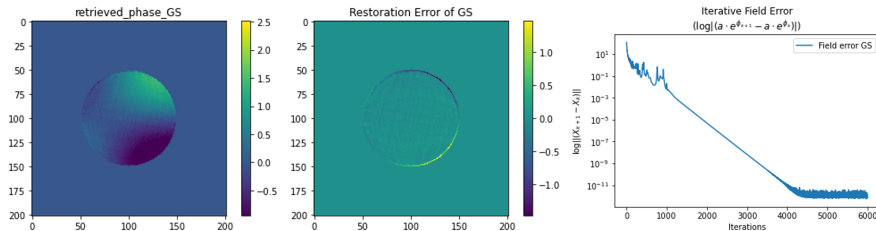

Figure 4-6: Retrieved phase of GS testing, RMSE error between restored and ground truth phase is 0.081. Left: Retrieved phase from GS algorithm; Middle: Restoration error between retrieved and ground truth phase; Right: Plot of iterative field error. This figure shows that the GS can restore the phase correctly.

We can now conclude that the implemented GS algorithm is functional in retrieving lower order phase. However the actual performance is subject to initial phase chosen. Some initial phase may result in poor retrieval performances, causing issues such as twin phase and sometimes residue phase when noise is present. These issues are partly because of no constraint is imposed in the alternative projection process, while phase retrieval itself is ill-posed and no unique solution is guaranteed, thus more than one phase can correspond to a intensity image. A few examples of such issues are shown in Figure4-7.
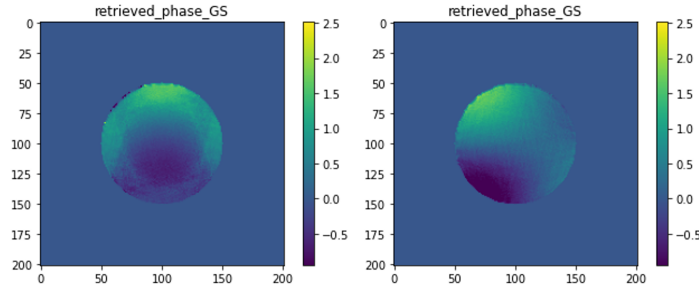
Figure 4-7: Examples of twin phases. Both phases are results from GS algorithm but with different initial guess. Both phases can reproduce a same PSF as input but far from ground truth phase, this is because of the non-uniqueness of the phase-intensity relation. This example shows the limits of GS algorithm and its dependency on initial guess.

4-2-2 PDPR-GS Algorithm

As discussed in section2-2-2 and shown in Figure4-7, GS algorithm along is not sufficient for the calibration of DM. To overcome some of its drawbacks, PDPR-GS is implemented. The process of PDPR-GS is shown in Figure4-8, similar to original GS algorithm, it projects field between 2 domains, with an extra information of known defocus phase ϕ_d added in the process.
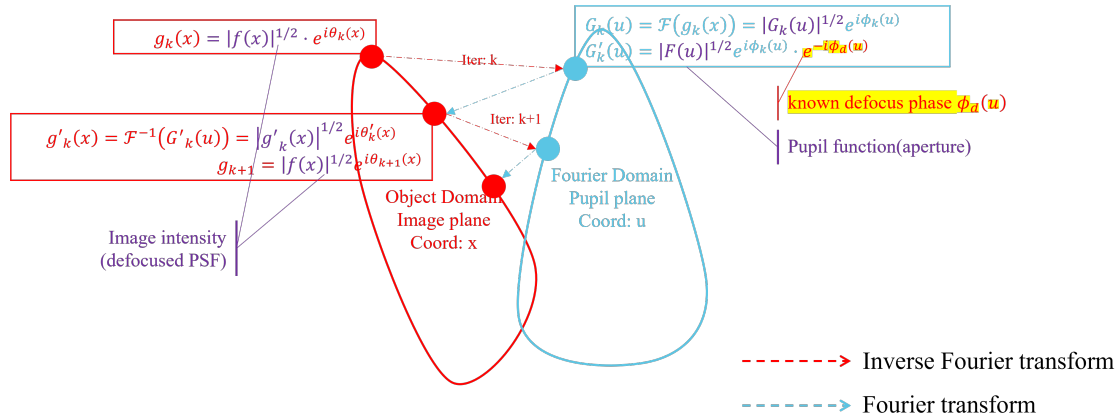

Figure 4-8: Illustration PDPR process as described in Algorithm2. Notations are followed from table2-1, implementation is listed in AppendixB-3.

For PDPR-GS, only a few more lines are needed compared to algorithm1, as shown in algorithm2.

To test the performance of PDPR-GS algorithm, we use a ground truth phase that is a combination of lower order Zernike mods and a response function of one actuator, and simulate the PSF as in the previous section. In able to compare the PDPR and pure GS algorithm, both methods are used to retrieve this phase. In addition to this, a defocus phase with maximum value of 0.75π is used as diversity phase in PDPR-GS. An PSF of ground truth phase added with this defocus phase is also simulated, as shown in Figure4-9.

Algorithm 2 PDPR-GS Algorithm

Given: measured intensity `|f(x)|`, measured diversity intensity `|f(x)_d|` Fourier plane intensity(aperture mask) $|F(u)|$, initial guess phase `phi_0` and diversity phase `phi_d`.

`p_0 = sqrt(|f(x)|)`: Square root of intensity measurement.
`p_d = sqrt(|f(x)_d|)`: Square root of intensity measurement with diversity phase added.
`a = sqrt(|F(u)|)`: Square root of aperture mask.
`g_k(x) = a * exp(phi_0 * 1j)`: Initial guess of field in the image plane.
while `k < max_iter` **do**
   `G_k(u) = fft2d(g_k(x)))`
   `G_k(u)_d = fft2d(g_k(x) * exp(phi_d * 1j)))`
   `g_k(x) = p_0 * exp(angle(G_k(u))`
   `g_k(x)_d = p_d * exp(angle(G_k(u)_d)`
   `G_k'(u) = ifft2d(g_k(x))`
   `G_k'(u)_d = ifft2d(g_k(x)_d * exp(-1j * phi_d))`
   `PDPR_phase = angle((G_k'(u) + G_k'(u)_d)/2)`
   `g_k(x) = ifft2d((g_k(x) + g_k(x)_d)/2)`
end while
Return: PDPR_phase

(a) Aperture mask used for PDPR and GS algorithm

(b) Ground truth phase for phase retrieval.

(c) Simulated PSF of ground truth phase.

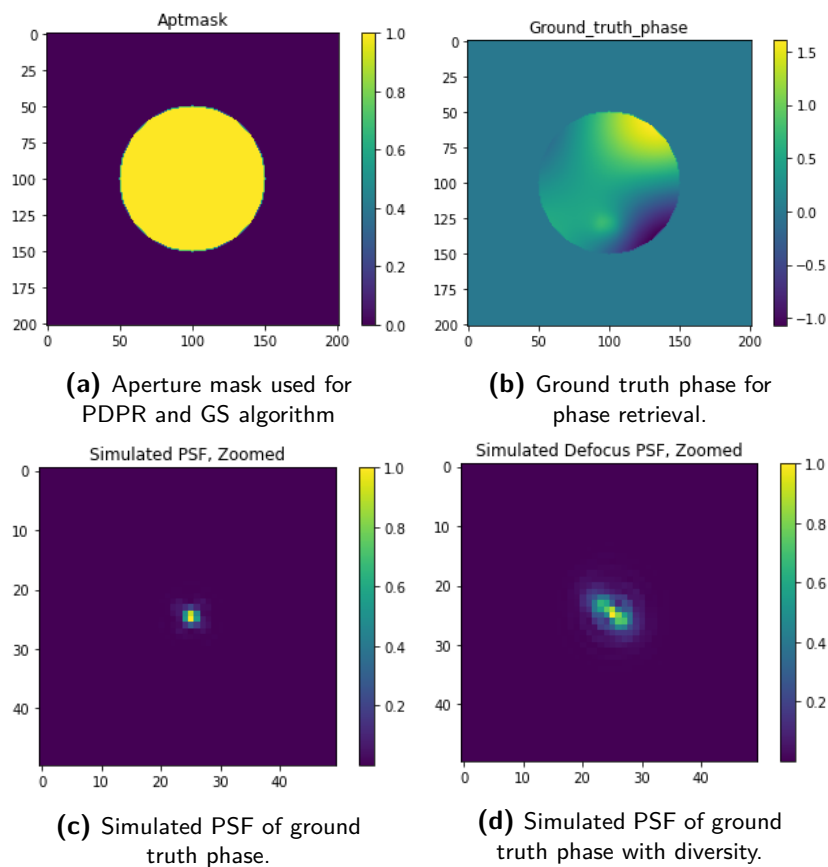**(d)** Simulated PSF of ground truth phase with diversity.

Figure 4-9: Setups for PDPR and GS testing. The new ground truth phase will be retrieved by PDPR and GS method for comparison.

The results of PDPR-GS are shown in Figure4-10, along with results from pure GS, both algorithms use a same initial phase. Error analysis of both phase retrieval methods are shown in Figure4-11. It can be seen that PDPR-GS has a higher accuracy and free from twin phase issues compared to pure GS. PDPR-GS sometimes converges faster than pure GS and sometimes not, depending on the initial phase and amount of defocus diversity used.

(a) Phase retrieved by GS algorithm. Twin phase.

(b) Phase retrieved by PDPR algorithm

(c) Restoration error between GS retrieved and ground truth phase.

(d) Restoration error between PDPR retrieved and ground truth phase.
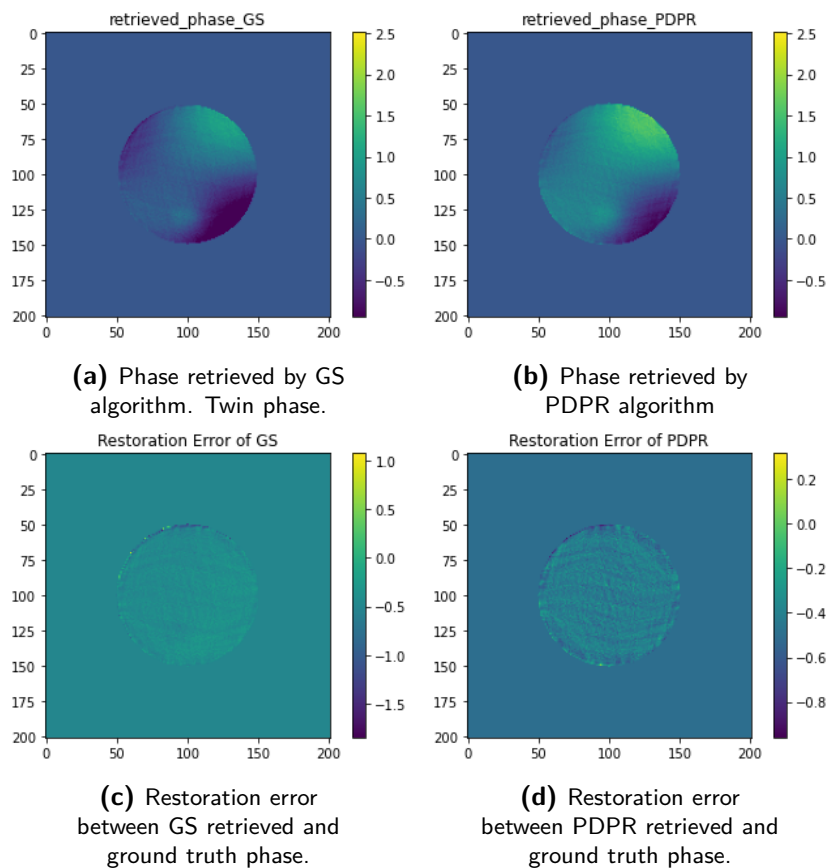
Figure 4-10: Phase retrieval results from GS and PDPR method. In GS method the phase is restored with larger error compared to PDPR reuslt. The GS retrieved phase is a twin phase in wrong direction, while PDPR retrieved phase is close to the ground truth. PDPR retrieved phase has RMSE of 0.082 while GS phase has an RMSE of 0.086. PDPR outperforms the GS in this case.
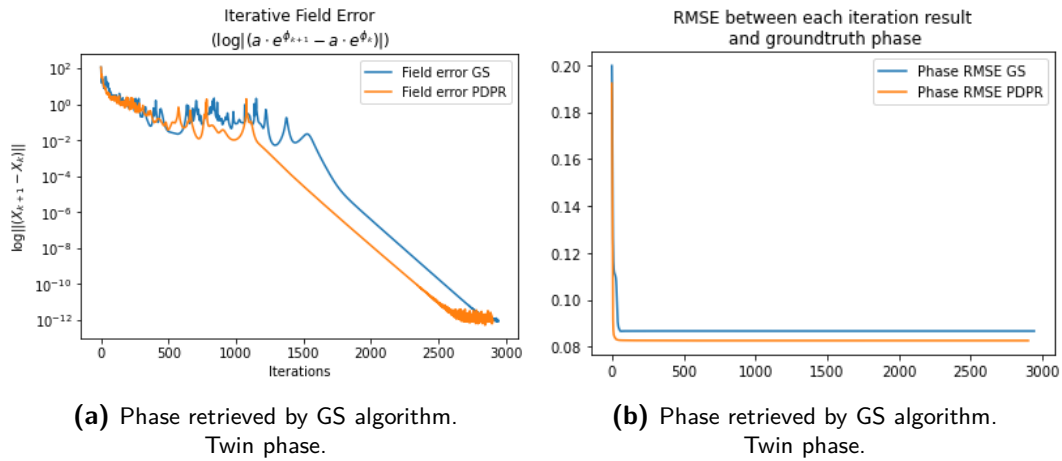
(a) Phase retrieved by GS algorithm. Twin phase.

(b) Phase retrieved by GS algorithm. Twin phase.

Figure 4-11: Iterative field error and RMSE between retrieved phase and ground truth phase. It can be seen that PDPR could converge faster than GS method, and has a higher accuracy than the GS method. It's worth noticing that the convergence rate of PDPR method largely depends on the diversity phase used while the accuracy of PDPR is always higher than GS. From this we conclude PDPR outperforms GS in terms of accuracy.

We can now conclude that the PDPR-GS algorithm performs better than GS in phase retrieval in the sense of accuracy and convergence rate. This motivates us to choose PDPR over GS for this project. Thus we have all the components needed for the simulation of DM calibration.

4-3 DM Calibration Simulation

To test the feasibility of proposed DM calibration scheme, a series of simulated calibrations are performed. This set of calibration makes use of the forward model and phase retrieval methods described above, as well as theoretical response functions of the DM provided by the manufacturer.

4-3-1 Theoretical Response Functions of DM

Theoretical response functions of DM is given by the manufacturer in the format of array of $200{\times}200$ size. Some of such response functions are shown in Figure4-12.
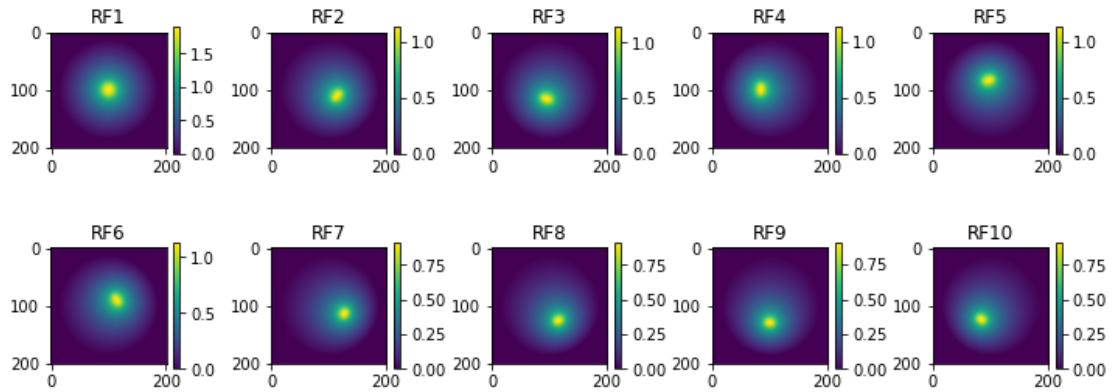
Figure 4-12: Examples of theoretical response functions (actuator#1-10). Obtained from manufacturer with size of 200×200 pixels.

To further check the response functions, add all the response functions with a same coefficient, extract all the non-zero points from this summed phase and use paraboloid curve fitting for it, as described in the following Algorithm3.

Algorithm 3 Analysis for response functions

Given: Theoretical response function of actuator #i RF_i

```
phase_map = ∑_{i=0}^{96} RF_i
def analytical_function = ax² + by² + c
analytical_surface = curvefit(analytical_function,phase_map)
Error = analytical_surface - phase_map
```
Return : Error

(a) Finding analytical surface of sum of response functions. Left: Sum of all response functions; Middle: extracted points from sum of response functions; Right: Analytical surface obtained by curve fitting the extracted points.

(b) Error between sum of RFs and analytical surface. Left: Analytical surface obtained by curve fitting; Middle: Sum of response functions; Right: Error between the two, shown the layout of actuators on the DM.
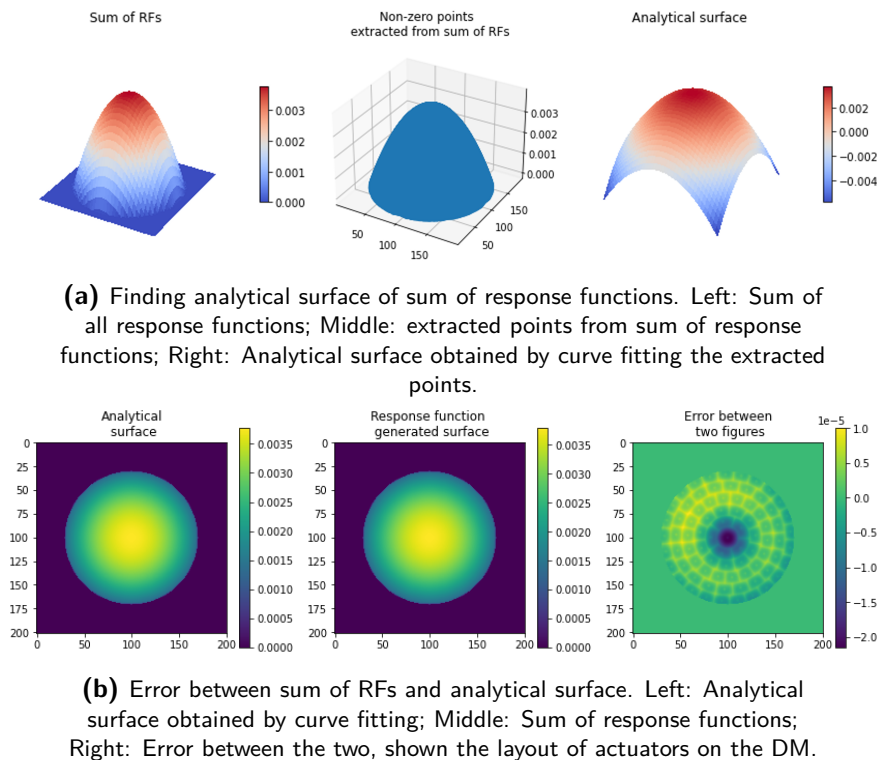
Figure 4-13: Print-through error.

The process and figures of Algorithm3 can be seen in Figure4-13, where the error between sum of response functions and analytical surface is shown. It can be seen that the error pattern corresponds to the layout of the actuators of the DM, as was shown in Figure3-2. This error is often referred to as "print-through" errors of the DM.

4-3-2 DM Calibration Simulation Process

The DM calibration simulation aims to reproduce the process of DM calibration on hardware setup as described in section3-1-3 from equation(3-5) to equation(3-9). Theoretical response functions for the DM added with noise are used to simulate the hardware DM performances. The simulation process is shown in Figure4-14.
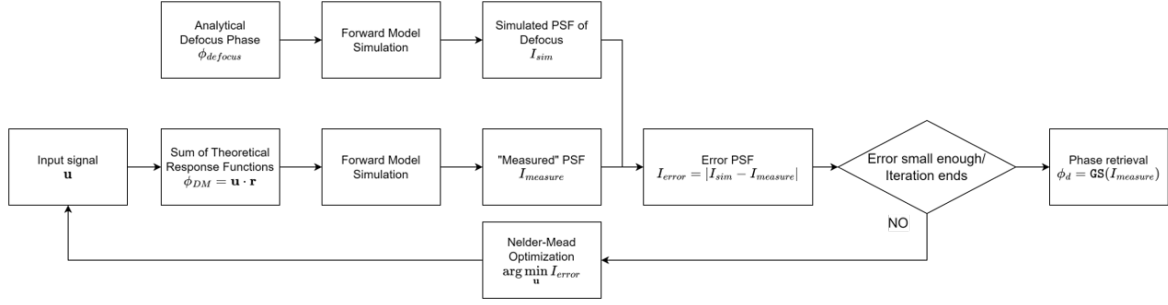
Figure 4-14: Simulated defocus calibration process that reproduces the defocus calibration as described in section3-1-3, using theoretical response function to replace real setup. Detailed explanation of this process can be found in section4-3-2.

Diversity Phase Calibration

First, an analytical defocus phase (Z_2^0) is generated. This phase is then padded to 1024×1024 which corresponds to the real setup. Denote this phase as $\phi_{defocus}$ as in section3-1-3. Then, forward simulate $\phi_{defocus}$ gives I_{sim} as in equation(3-5), results are shown in Figure4-15. This is the ideal PSF which the setup should give.

After this, a set of theoretical response functions is used to simulate the performance of DM. Denote the input signal and response function of actuator i as u_i and r_i, equation(4-11) gives the output phase ϕ_{DM} of DM. The initial values of u_i are set to zeros, which corresponds to zero input to the DM. Note that the theoretical response functions r_is are used here only to simulate the DM, and are regarded as unknown for all other cases.

$$\phi_{DM} = \sum_i^N u_i \cdot r_i. \tag{4-11}$$

We then use forward model again to get the simulated "measured" PSF, as described in equation(4-12):

$$I_{measure} = \texttt{Simulation}(\phi_{DM}). \tag{4-12}$$

Then, as denoted by equation(3-6), an optimization program based on Nelder-Mead and minimizes the spot width of the error PSF between simulated and 'measured' PSFs is performed. This iterative process manipulates the DM inputs $\mathbf{u}$ until a signal $\hat{\mathbf{u}}$ that generates a PSF that is closest to I_{sim} is obtained. The optimization results are shown in Figure4-16.

Having obtained $\hat{\mathbf{u}}$ from optimization, use GS to retrieve the diversity phase ϕ_d of the $I_{measure}(\hat{\mathbf{u}})$ as in equation(3-7).

Having obtained the optimized input signal $\hat{\mathbf{u}}$, the configuration of simulation is then changed. With phase map size changed from 1024×1024 to 201×201, and aperture radius of 50. The reasons for this change are as followed. Firstly, a larger (padded) phase map would give a finer PSF image, which is good for PSF based optimization, since the input signal $\hat{\mathbf{u}}$ is now obtained, the necessity of using a high-resolution PSF drops. Secondly, using a 1024×1024 phase map requires long computation time for phase retrieval, while 201×201 size phase map

(a) Analytical defocus phase $\phi_{defocus}$, padded in accordance with the setup.

(b) Analytical defocus phase, padded in accordance with the setup, zoomed.

(c) PSF of analytical defocus I_{sim}, simulated by forward model.

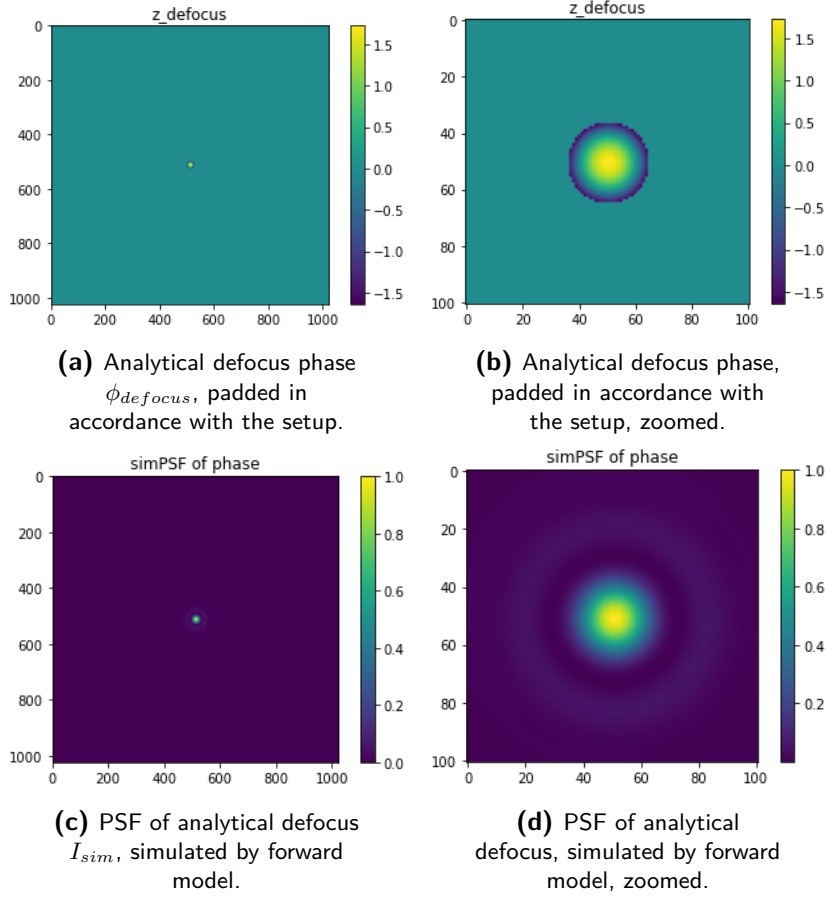**(d)** PSF of analytical defocus, simulated by forward model, zoomed.

Figure 4-15: Analytical defocus phase $\phi_{defocus}$ and simulated PSF I_{sim} of it. Simulated using forward model corresponding to modified setup as shown in Figure3-4b, with padding size of 1024×1024 and Q-factor of 20.

takes shorter time with acceptable results. Since the aim of this numerical simulation is to validate feasibility of the proposed characterization method, it is more desirable to get the results faster than finer.

The GS retrieved phase ϕ_d from PSF $I_{measure}(\hat{\mathbf{u}})$ is shown in Figure4-17. It can be seen that the reconstructed ϕ_d has lots of noise, ϕ_d is close to ϕ_{DM} but not so close to $\phi_{defoucs}$ as desired. The RMSE between phi_d and ϕ_{DM} and $\phi_{defocus}$ are 0.20 and 0.57 respectively. However, the ϕ_d can still be used in the phase diversity algorithm since its fully known and has a corresponding input signal.

DM Calibration

With diversity phase and corresponding input signal obtained, we are ready for calibrating the deformable mirror using Phase Diversity Phase Retrieval (PDPR) method. The process of simulated DM calibration is shown in Figure3-5 and as described in section3-2.

The simulated characterization results are shown in Figure4-18 at the end of this chapter. Here theoretical response functions as well as step response of each step of each actuator is
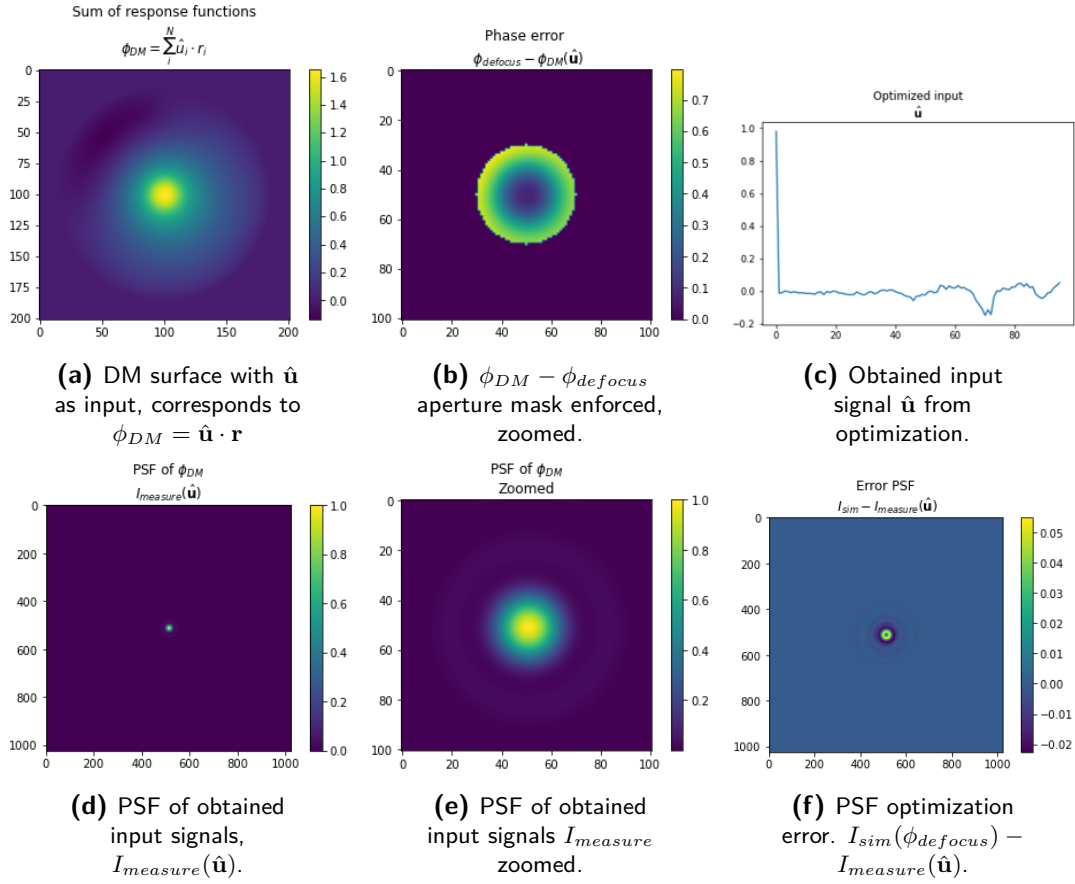
(a) DM surface with $\hat{\mathbf{u}}$ as input, corresponds to $\phi_{DM} = \hat{\mathbf{u}} \cdot \mathbf{r}$

(b) $\phi_{DM} - \phi_{defocus}$ aperture mask enforced, zoomed.

(c) Obtained input signal $\hat{\mathbf{u}}$ from optimization.

(d) PSF of obtained input signals, $I_{measure}(\hat{\mathbf{u}})$.

(e) PSF of obtained input signals $I_{measure}$ zoomed.

(f) PSF optimization error. $I_{sim}(\phi_{defocus}) - I_{measure}(\hat{\mathbf{u}})$.

Figure 4-16: Results of PSF optimization for generating diversity. In Figure4-16a the whole surface of DM is shown while only the central working aperture part is used, as in Figure4-16b. The results indicate that the PSF optimization can obtain a $\hat{\mathbf{u}}$ that reproduce $\phi_{defocus}$ to some extend but not entirely same. Changes in input signal $\hat{\mathbf{u}}$ is very limited especially for actuators in inner rings.

shown. The analysis of the characterization results will be presented in the next section.

4-3-3 DM Calibration Simulation Results

To take a closer look at the obtained response functions in Figure4-18, we choose one actuator as an example. As shown in Figure4-19a the simulated characterization results for actuator #8. Step 1-5 indicates the characterization results for each step number.

It can be seen that the characterization results are in line with the theoretical response functions. The error between the obtained ϕ_c^8 and theoretical r_8 is small.

However in steps such as 1,4,5, there are obvious fish-scale patterns while others not. This is because GS is heavily dependent on the starting point and some starting point would give better convergence results and some not. Such patterns are expected in the GS-class phase retrieval methods. If one were to get rid of such patterns, one can use several different starting phase and choose the one with best result, however this would make the simulation time significantly longer.
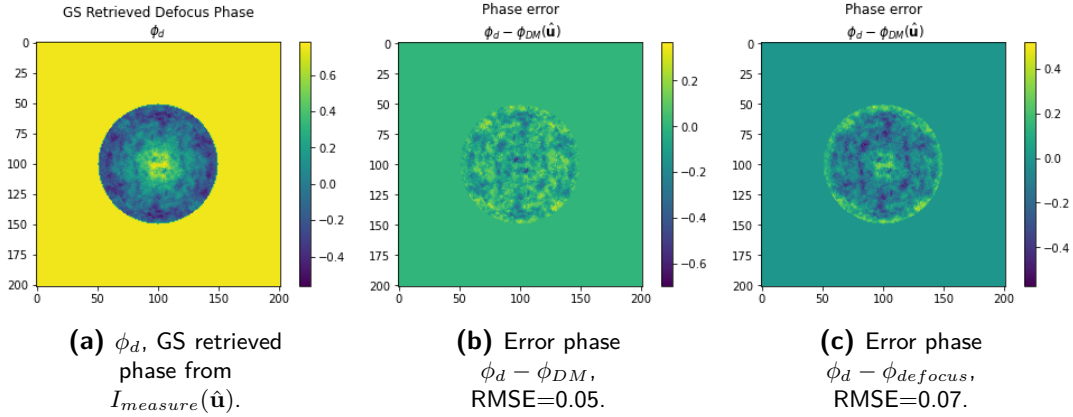
(a) ϕ_d, GS retrieved phase from $I_{measure}(\hat{\mathbf{u}})$.

(b) Error phase $\phi_d - \phi_{DM}$, RMSE=0.05.

(c) Error phase $\phi_d - \phi_{defocus}$, RMSE=0.07.

Figure 4-17: The GS retrieved phase ϕ_d from PSF $I_{measure}(\hat{\mathbf{u}})$. To reduce computation time, the simulation configuration in this figure is slightly different from that in Figure4-16. The phase retrieval result is not optimal but can still be further used for DM characterization.
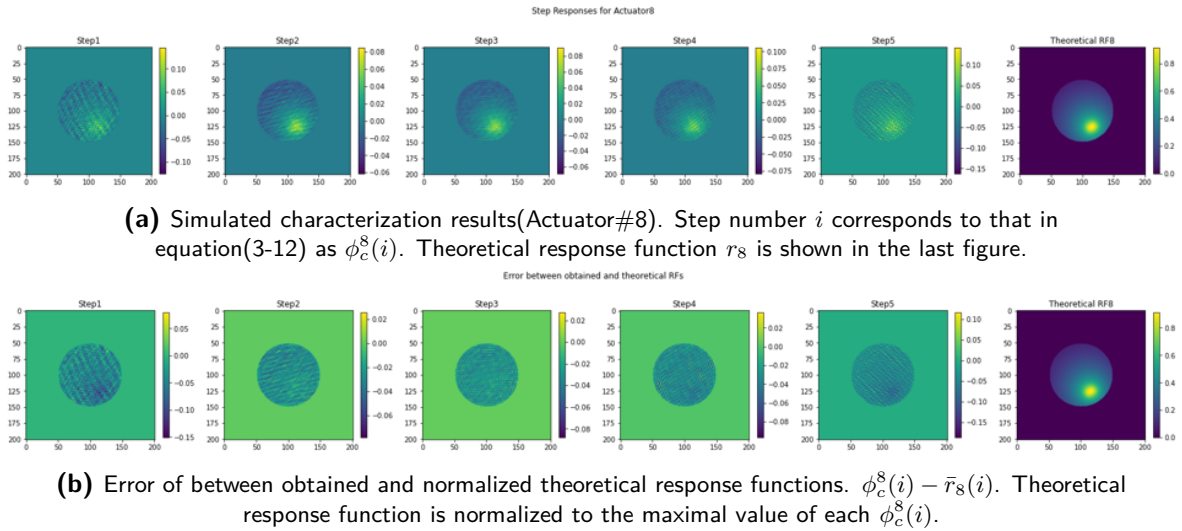

(a) Simulated characterization results(Actuator#8). Step number i corresponds to that in equation(3-12) as $\phi_c^8(i)$. Theoretical response function r_8 is shown in the last figure.

(b) Error of between obtained and normalized theoretical response functions. $\phi_c^8(i) - \bar{r}_8(i)$. Theoretical response function is normalized to the maximal value of each $\phi_c^8(i)$.

Figure 4-19: Simulated characterization results(For actuator#8). Despite of the presence of noise, characterization result matches that in theoretical response functions.

In Figure4-20a, the average of RMSE between theoretical response function and each step response is shown. The average RMSE value for each actuator is calculated as shown in equation(4-13): first calculate the RMSE between obtained step response $\phi_c^k(i)$ and theoretical response function r_k, repeat for all M steps, then calculate the mean of RMSE of all steps.

$$\text{RMSE}_k = \frac{\sum_i^M \text{RMSE}(\phi_c^k(i), r_k)}{M}. \tag{4-13}$$
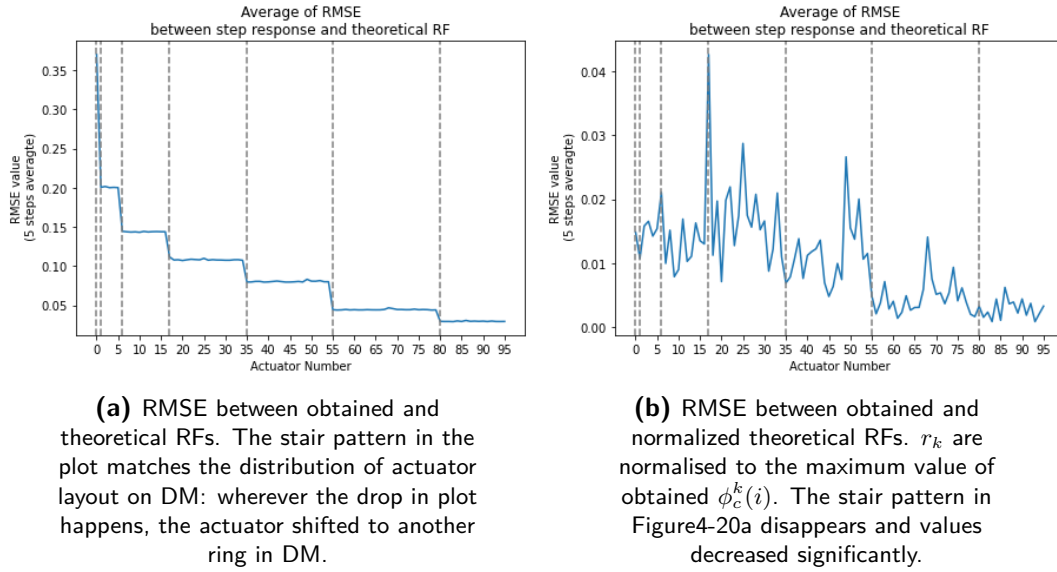
(a) RMSE between obtained and theoretical RFs. The stair pattern in the plot matches the distribution of actuator layout on DM: wherever the drop in plot happens, the actuator shifted to another ring in DM.

(b) RMSE between obtained and normalized theoretical RFs. r_k are normalised to the maximum value of obtained $\phi_c^k(i)$. The stair pattern in Figure4-20a disappears and values decreased significantly.

Figure 4-20: RMSE between obtained ϕ_c^ks and theoretical r_ks. Left: RMSE plot of each actuator without r_k normalization. Right: RMSE plot of each actuator with normalized r_k.

As is shown in Figure4-20a, the RMSE between obtained and theoretical response function drops as actuator number increases. The drop happens only when the actuator is further from the center, i.e., RMSE stays the same for all actuators on the same ring. This matches the layout of the actuators on the DM. The cause for such trend is the scale of theoretical response functions are not normalized, as all response functions are obtained using the same voltage step difference, the further the actuator is from the center, the smaller scale of deformation per unit step difference can make.

In Figure4-20b where the theoretical response functions are normalized to the scale of obtained step response, the trend disappeared and RMSE values dropped significantly.

As is shown by the results, the proposed PDPR based characterization process is in principle attainable. The RMSE could reach ≤ 0.04, depending on the choice of initial guess of phase, while for the majority of the actuators the RMSE is well below 0.02.

4-4   Conclusion

In this chapter, all the essential parts of carrying out the characterization have been built, including a forward model, Gerchberg-Saxton based Phase Diversity Phase Retrieval algorithm and theoretical response functions have been inspected, a simulated characterization process is also demonstrated.

The forward model built is capable of reproducing image formation process of the setup as simulated Airy disc pattern matches that in the setup measurement. The GS algorithm is also functional for phase retrieval and its performance is dependent on initial guess of phase. The GS based phase diversity phase retrieval algorithm is also functional and out performs the original GS as it eliminates the possibility of twin phase.

A simulation based DM characterization is also performed in this chapter. Using theoretical response functions as the simulated setup with Gaussian noise added to the PSF registering step, the proposed scheme is capable of retrieve phase for each step of input and obtain response functions of each step. The RMSE error between retrieved response functions and theoretical values could reach approximately 0.02 for most of the actuators.

It is then argued that the proposed characterization scheme is capable of characterizing the DM. In the next chapter, the characterization scheme will be tested on the experimental setup.
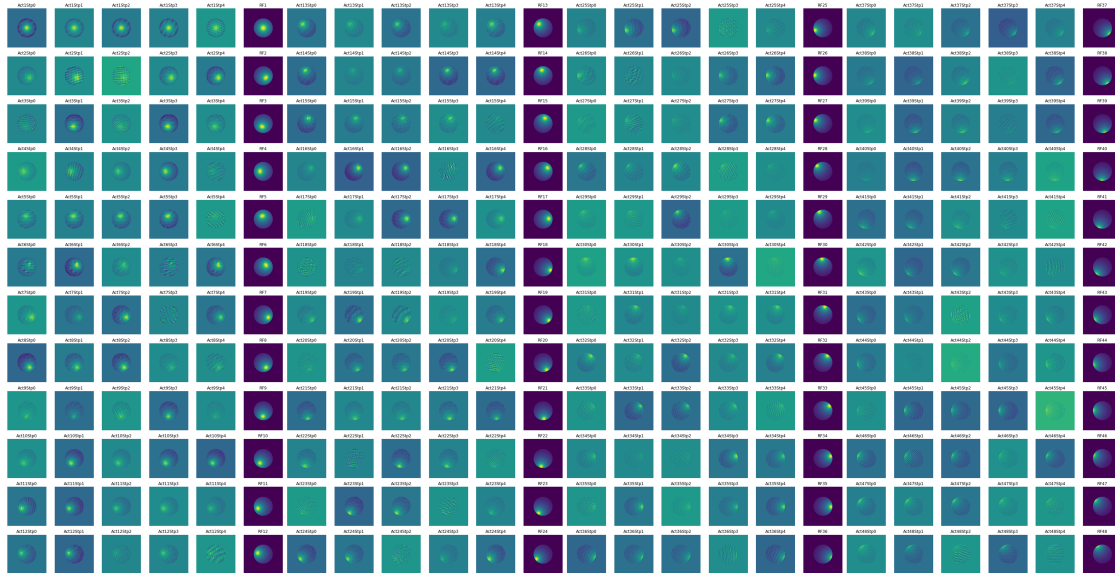
(a) Simulated characterization results(Actuator#1-48).
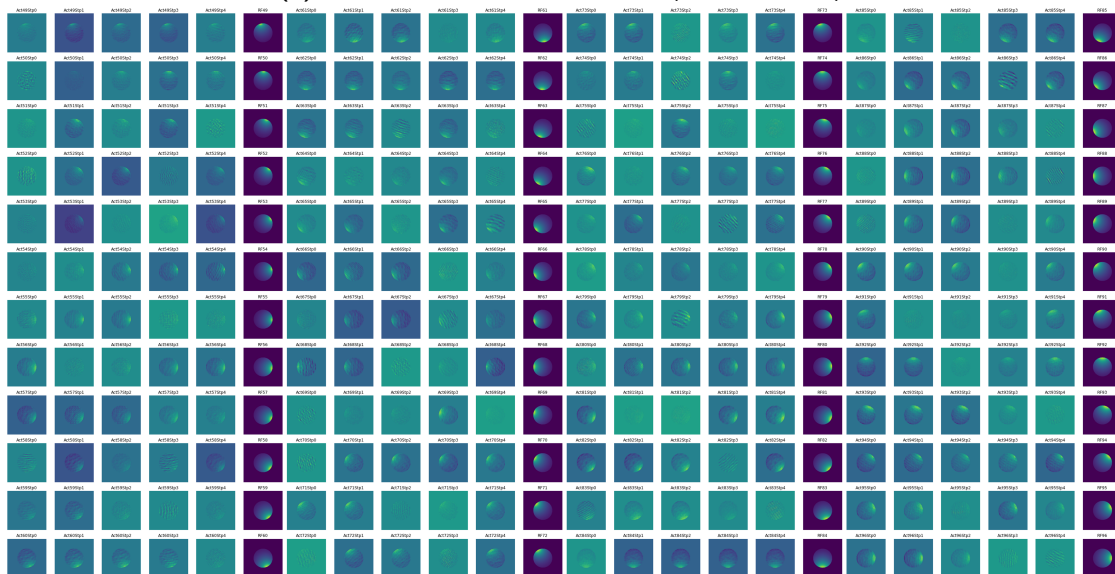
(b) Simulated characterization results(Actuator#49-96).

Figure 4-18: Simulated characterization results. For figures with higher resolution see Appendix FigureA-1, A-2 and A-3.

Chapter 5

DM Calibration on Hardware

To test the performance of the proposed calibration method even further, a set of experiments on a AO setup is performed. In this chapter, the experimental setup is first introduced, following a description of the experiment procedures, and then the calibration results and analysis.

5-1 Experimental Setup

The setup used for experiments is introduced in section3-1-2 and Figure3-4. Apart from the hardware, there are more to be specified including the PSF registration and alignment issues, which would be treated in this section.

5-1-1 PSF Registration

For a PSF taken from the camera, it is desirable that the image patterns to be bright and clear and with minimum noise. The image should also not be overexposed otherwise information would be lost.

For this purpose, the PSF registration process is designed to have the pixel value between 180-240 gray scales. An example of PSF registration is shown in Figure5-1a.

After taking the PSF from the camera, a few steps are taken to make the image more suitable for phase retrieval algorithm. The measures taken are summarized as follows.

Cropping : The camera image is of 1280×1024 pixels, which is usually too large for a PSF. To reduce noise in edge areas the camera image is cropped around the brightest point.

Normalizing : The camera image is of 8-bits or 255 gray scales. To normalize the image between 0 and 1, all pixel values are divided by 255.
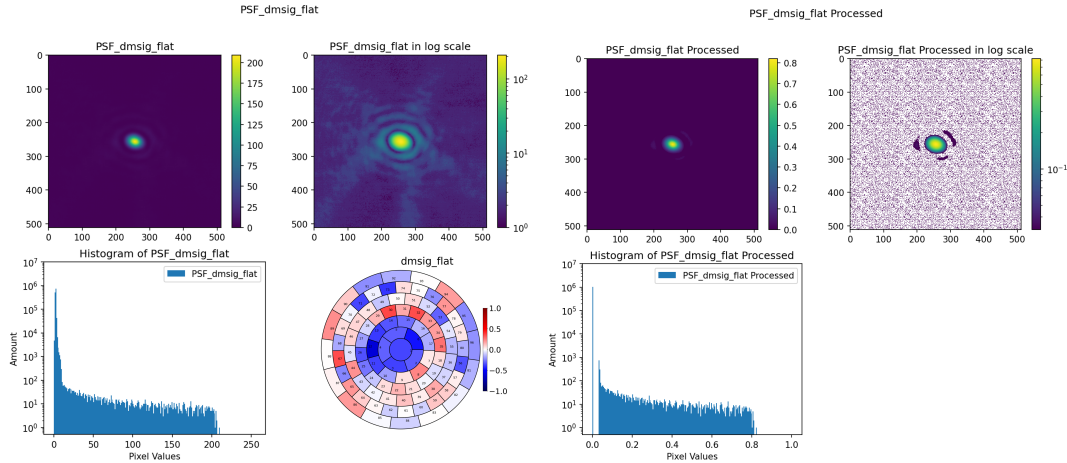
(a) Example of PSF registration.
Upper left: camera image; upper right:
camera image in logarithm scale; lower
left: histogram of camera image; lower
right: DM input signal.

(b) Example of processed PSF.
Upper left: processed camera image;
upper right: processed camera image in
logarithm scale; lower left: histogram of
processed camera image.

Figure 5-1: Example of PSF registration and process. Left: raw camera measurement; right:
processed camera measurement. PSF process measures include cropping, normalizing and
thresholding.

Thresholding : The camera image would be used for GS based algorithms which are sensitive to intensity noise. To reduce the noise and improve the phase retrieval performance, a threshold of 0.03 is used. This empirical threshold would filter out most high frequency noise while not losing too much information.

Another method that could be adapted is to take several PSFs and then average them as the final PSF. However this does not always ends in better performance and has little influence on the phase retrieval results and thus not adapted.

An example of processed PSF is shown in Figure5-1b. It can be seen that the noise in the logarithm figures are significantly less while the original PSF pattern is preserved.

5-1-2 Alignment

Another issue to be addressed is the alignment. Ideally the DM would compensate for the initial aberrations in the setup thus lower the requirements for alignment. However, as shown by experiment, DM cannot compensate for any arbitrary aberrations. Especially when the setup is misaligned, no matter how many iterations were performed, the PSF pattern is always highly aberrated.

A direct result of un-removable aberration is the difficulty in phase retrieval. As shown in Figure5-2, when the PSF is highly aberrated, the retrieved phase is full of artifacts and noise. No matter what PSF pre-process measures are taken, the phase retrieval results are still invalid.
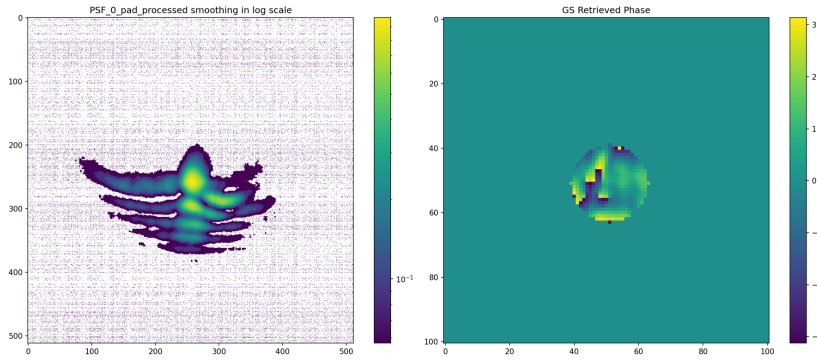
Figure 5-2: An extreme example of PSF from misaligned setup.
Left: processed PSF; right: retrieved phase. This example is used to emphasize the importance of good alignment.

During alignment, it is important to ensure the camera is properly located in the focus of incoming light. An empirical metric for this is to check the input signal that makes the DM "flat." A "flat" signal is obtained using BeamTuner software from Flexible Optical.B.V., where irregular simplex and Nelder-Mead are used to minimize the spot width. When the central actuators in the obtained "flat" signal have almost 0 voltage, the camera is in focus, when the central actuators have large inputs, the camera is not. As shown in Figure5-3.
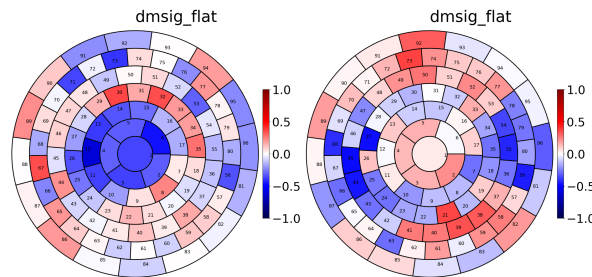
Figure 5-3: "Flat" signals for different camera position.
Left: camera out of focus; right: camera in focus.
When the input value of central actuators in "flat" signal is approximately 0, we conclude that the camera is in focus of incoming beam.

5-2   Diversity Phase Calibration

In this section, the acquisition of diversity phase to be used in Phase Diversity Phase Retrieval (PDPR) would be presented. Following from section3-1-3, there are 2 ways of generating and calibrating a diversity, i.e., via PSF optimization and unified DM input. In this section, both method have been tested and the unified input method is chosen at last.

5-2-1   Diversity Phase Acquisition via PSF Optimization

The process of diversity acquisition via PSF optimization is introduced in section3-1-3. A simulation of this method is given in section4-3-2. In this subsection, the diversity acquisition is performed on the real setup. The optimization results after 5000 iterations are shown in Figure5-4.
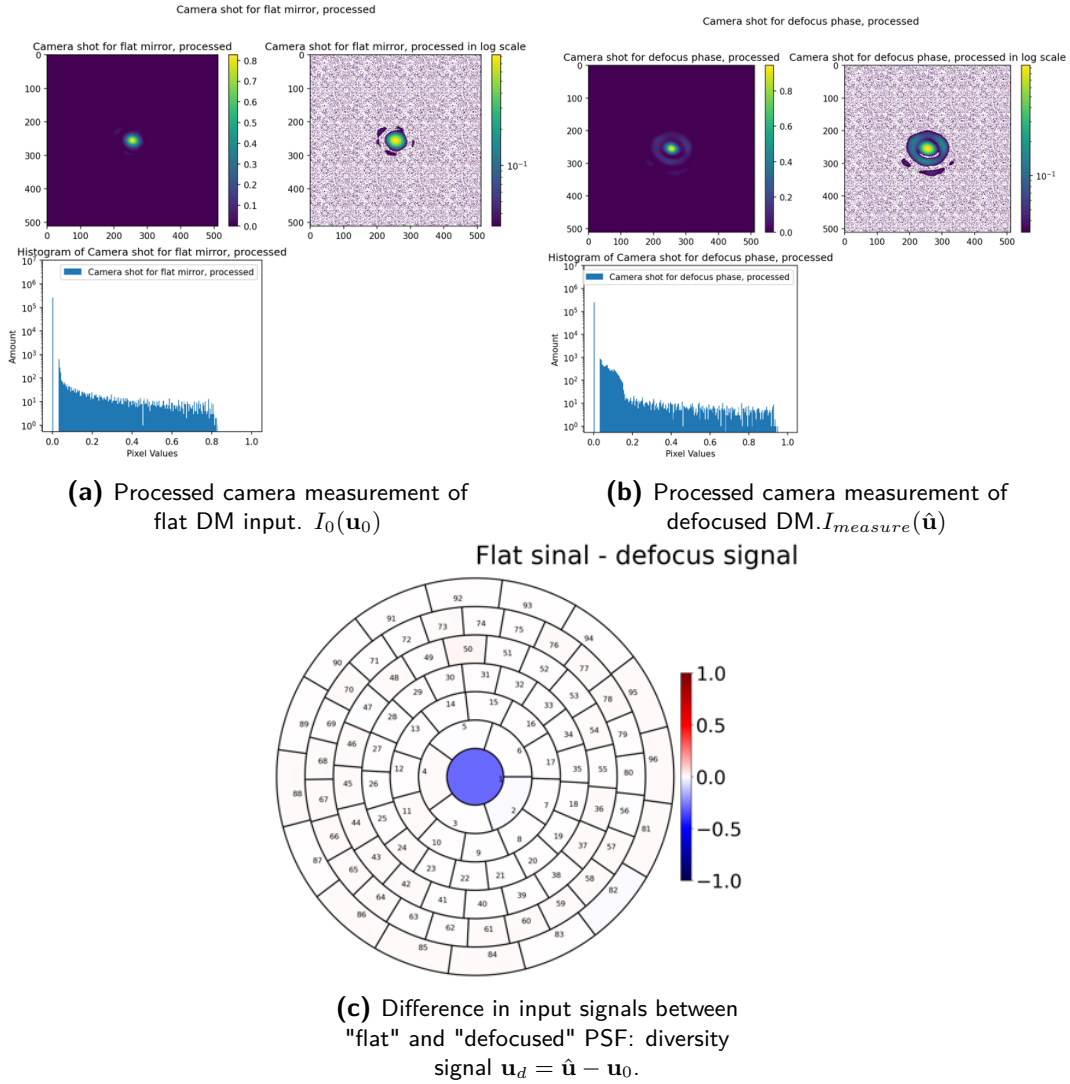

(a) Processed camera measurement of flat DM input. $I_0(\mathbf{u}_0)$

(b) Processed camera measurement of defocused DM. $I_{measure}(\hat{\mathbf{u}})$

(c) Difference in input signals between "flat" and "defocused" PSF: diversity signal $\mathbf{u}_d = \hat{\mathbf{u}} - \mathbf{u}_0$.

Figure 5-4: Results of PSF optimization. It can be seen that the optimized input signal $\hat{\mathbf{u}}$ is not so different from the flat mirror input. This is inline with the simulation results as shown in Figure4-16d in section4-3-2.

As is shown in Figure5-4, the resulting diversity signal$(\hat{\mathbf{u}} - \mathbf{u}_0)$ is similar to that in the simulation case, as was shown in Figure4-16 in section4-3-2.

Then, followed from equation(3-3) and equation(3-4), the diversity phase can be determined. As shown in Figure5-5. Saving the pair of phase input signal $\phi_d, \mathbf{u}_d$, we are ready to use PDPR for characterization. This method of obtaining a known diversity phase seems to be
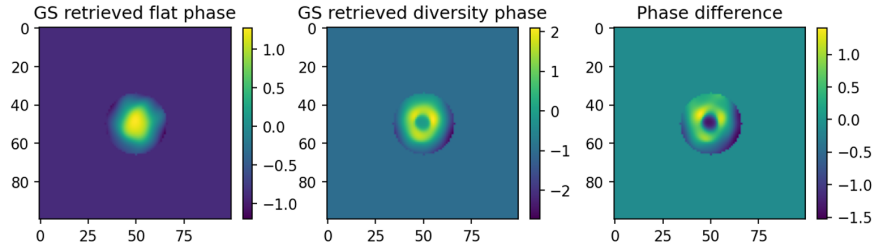
Figure 5-5: GS results on measured PSFs.
Left: GS retrieved flat phase ϕ_0; middle: GS retrieved defocused phase $\phi_{defocus}$; right: diversity
phase $\phi_d = \phi_0 - \phi_{defocus}$.

functional and gives proper results. However this method is not adapted at last due to a series of issues including instability of the setup which would be treated in later section5-4. The diversity phase is obtained using unified actuator input as discussed in the next subsection.

5-2-2   Diversity Phase Acquisition via Unified Actuator Input

As shown in the previous section, PSF optimization is a possible way to obtain a diversity phase. However this path is not chosen, partly because it takes long time to run PSF optimization and the resulting phase is not strictly defocus.

Knowing that as long as a diversity phase is constant and known, it can be used in PDPR algorithm. Following the steps in section3-1-3, unified actuator input is used for diversity phase calibration.

The unified actuator input $\mathbf{u}_d$ should be neither too large nor too small, so that the PSF can be retrieved properly. Set 0.05 for all actuators inside a certain ring and 0 for all others, as shown in Figure5-6. The phase retrieval results $\mathbf{u}_d$ and ϕ_d to be used in PDPR are also shown in the last column of this figure.

5-3   DM Characterization Results

In this section, the first round of DM characterization is carried out following the procedures described in section3-2. After a brief analysis of the results, another round of characterization is performed again with updated settings.

5-3-1   First Characterization Results

The characterization results

Using all the components and process mentioned above the first 32 actuators characterization results are shown in Figure5-7.
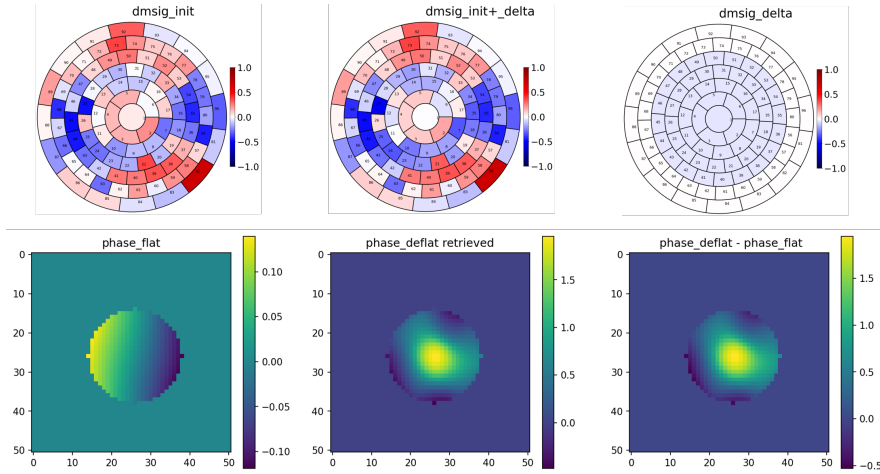
Figure 5-6: Input signals and retrieved phase for diversity phase calibration.
Upper left: flat signal $\mathbf{u}_0$; upper middle: flat signal added by diversity signal $\mathbf{u}_1 = \mathbf{u}_0 + \mathbf{u}_d$;
upper right: diversity signal $\mathbf{u}_d$
Lower left: GS retrieved phase ϕ_0 for flat signal $\mathbf{u}_1$; lower middle: GS retrieved phase ϕ_1 for
signal $\mathbf{u}_1$; lower right: diversity phase $\phi_d = \phi_1 - \phi_0$

Results analysis

As is seen in Figure5-7, the characterization results in general match the theoretical response functions. However there are a few issues to be noticed. Having a closer look at, for example, actuator #24, as shown in Figure5-8, for all steps the obtained response functions have a similar pattern in a similar position as the theoretical response function.

However in some steps there are more obvious noise or artifacts. The possible cause for such differences between each steps are various, including the noise in the measurement which influence the phase retrieval process, the non-linearity of DM's deformation with linearly changing input signal, and instability of the laser source.

Indications for misalignment

Noticing that there is always difference in position of the patterns from characterization and theoretical response function, as shown in Figure5-9. Such discrepancy in position indicates that the DM is not posed strictly in the center of incoming light beam, indicating presence of misalignment. Given more time, such positional displacement can be further verified using correlations between obtained and theoretical response functions.

Time consumption

It is worth mentioning that the actual time used is significantly shorter than expected. Starting from a random initial phase, PDPR algorithm can converge in approximately 300 iterations, then, use phase retrieval result of previous step as initial guess in next step, the algorithm can converge within 50 iterations. Using an average PC with i7-4790 3.6GHz CPU, GS speed for an 512×512 figure is approximately 4 iterations per second, for 1024×1024 figure
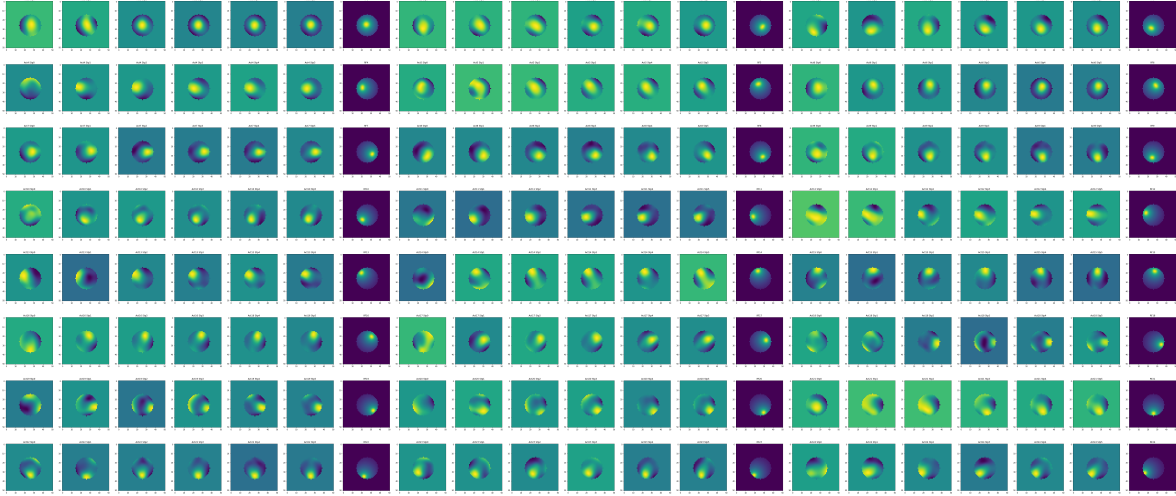
Figure 5-7: Characterization results on setup, for actuator#1-24. For higher resolution figures and remaining actuators see Appendix FigureA-4.The characterization results visually match that in the theoretical response functions.
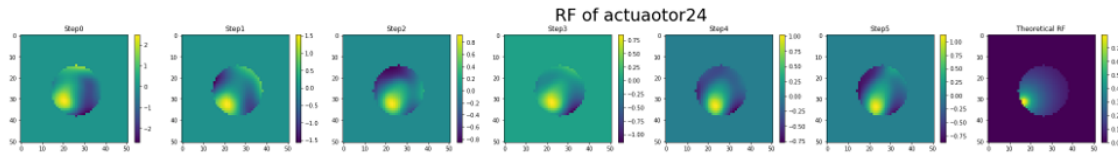

Figure 5-8: Characterization results for actuator #24. This example is used to show the characterization result matches theoretical response function, with acceptable level of noise and position mismatch.

approximately 1.5 iteration per second. Supposing 10 input steps are used, this means that for a smaller figure, characterization time could reach $\sim$ 4min per actuator and $\sim$ 10min for larger figure. Besides, the PSF registration and PDPR can happen asynchronously, allowing for using computers with higher performance to run the phase retrieval program.

Second derivative analysis

To further inspects the characterization results, Laplacian of obtained response functions is calculated. Ideally, the Laplacian of a response function could show the shape of the actuator, as shown by the second derivative of theoretical functions in Figure5-10.

As is shown, Laplacian of obtained response functions follows the trend of that in theoretical ones. However in obtained response functions, there are more artifacts than that in theoretical ones. There is not only the shape of desired actuator, but also shape of other actuators, as if not only the desired actuator is given an input step, but all actuators on the same ring is given an input step.

The current characterization results are too small in size and a lot of details are lost. To compensate for this, another round of characterization, with padding size doubled from 512 to 1024 pixels has been performed. It will be treated in the following section.
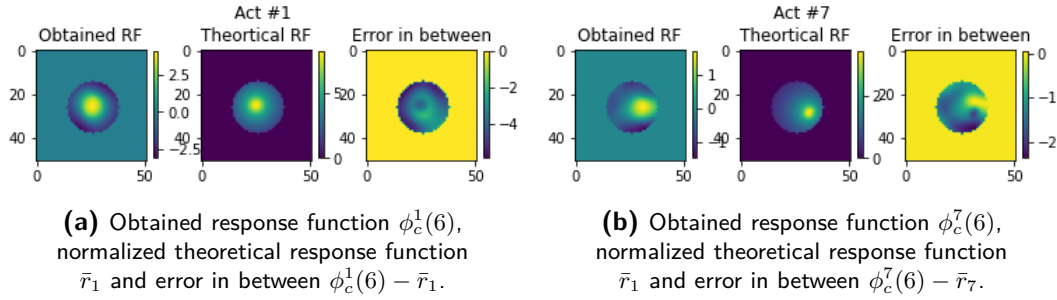
(a) Obtained response function $\phi_c^1(6)$, normalized theoretical response function $\bar{r}_1$ and error in between $\phi_c^1(6) - \bar{r}_1$.

(b) Obtained response function $\phi_c^7(6)$, normalized theoretical response function $\bar{r}_1$ and error in between $\phi_c^7(6) - \bar{r}_7$.

Figure 5-9: Error between theoretical and characterization results. For all other actuators see AppendixA-5. Error between characterization results and theoretical functions indicate the presence of misalignment. The pattern in error phase map, especially in Figure5-9b, are because of DM not in the center of incoming beam.

5-3-2   Characterization Using Modified Settings

Using updated characterization settings of larger image/padding size, a new round of characterization has been performed, results for the first 2 rings(actuator#1-6) are shown in Figure5-11.

It can be seen that the characterization results are of higher resolution compared to previous one. Results also match the patterns in theoretical ones. However it can also be seen that there are even more noise and artifacts when compared to smaller padding settings.

This is more obvious in the second derivative figures. For example in actuator15 as shown in Figure5-12, for the second derivatives, it is quiet obvious that there is a pattern matches that in the theoretical response function, but there are also lots of other artifacts that seemingly like shapes of other actuators. Such situation is present in results of all actuators being characterized. The possible cause for such unexpected patterns and artifacts are discussed in the next section.

5-4   Results Analysis

5-4-1   Further characterization attempts

In previous characterization results, it often happens that in the second derivative there seems to be more than one actuator acting, or that the setup is not behave as commanded. To further investigate this, we first use a same set of configurations to characterize a single actuator multiple times and check whether the results are in line with each other.

As shown in Figure5-13, the characterization results are not the same for different rounds. For instance in the number of artifacts are different in each round, as well as. This is not as expected and indicates that there might be some issue with the setup itself. In an ideal case, no matter how many time a certain actuator is characterized using a same configuration, the characterization results should stay the same.

To further analysis the properties of the setup, we tried to characterize the DM per ring, i.e., to run the characterization procedure not to a single actuator, but to all actuators that are

in the same ring. Results are shown in Figure5-14. It can be seen that the results are quiet noisy and the shape of rings are vague. For ring#3, the second derivative pattern are closer to the shape of ring of actuators, however there is always a bright spot in the center.

5-4-2 Investigating setup performance

DM Stability Issues

The characterization results suggest that the setup might not be stable. An observation of instability of the setup is related to "flat mirror" optimization mentioned earlier. Ideally the input signal that makes the DM flat would be almost the same throughout time, however in reality it's not like this. As shown in Figure5-15, throughout time, for the very same setup with same settings and same BeamTuner software that does the optimization job, the resulting input signal changes a lot. Especially for the actuators in the first ring(actuator#1-6), the deviation can be as high as 0.25. This is a very large scale for input signals, as they are normalized between -1 and 1, and in characterization the step size is usually no more than 0.15.

This observation means that to obtain a same DM shape, the control signal has to change over time and vice versa. This suggests that the position of DM's central actuators might move and thus the performance of a same control input would vary.

Humidity Issues

Another possible influencing factor is the humidity level near the setup. It was not noticed until the later part of this thesis that the humidity level in the laboratory varies a lot. An example of the varying humidity level is shown in Figure5-16, the humidity level is far from stable and can change up to $\sim 40\%$. Though the influence of environmental factors is out of the scope of this thesis, as suggested by Ref[32], humidity level would largely influence the performance of the DM, as membrane could take water vapor from air and reduce the tension in the membrane and thus changing the spring constant restoring force. In other words, changes in humidity level would result in changes DM's response function.

Laser-Camera Issues

To investigate all possible issues that might lead to the undesired setup performance, the camera and laser are also checked. To perform this check, the DM is shut off to exclude any possible fluctuation the DM could make. Then, take a series of shots with time interval of 0.5s. Subtracting two consequent shots and the results are shown in Figure5-17.

It can be seen that there is an obvious PSF pattern, which indicates that each time the camera read out is different. Such pattern is small in scale in the beginning and gets larger and larger as time passes. This means the lasercamera is also not constant overtime, which could lead to undesired characterization results.

5-5 Conclusion

In this chapter, the implemented characterization scheme is tested on real setup. Initial steps include carefully align the setup, set camera exposure to a proper range and using an extra unified actuator input to generate diversity phase and calibrate it using GS algorithm.

After this, the first characterization results are obtained, which showed the response functions of first 32 actuators. The shape of response function matches that in the theoretical response functions, this shows that the proposed characterization scheme is attainable and promising. Second derivative of phase is used to validate the results. Analysis of the results shows that during alignment the DM is not put strictly in the center of the light beam. However in this round of characterization the padding used is too small and we could not see too much details in the results.

For this reason another characterization is carried out with padding size doubled. In this characterization, the results still matches that in the theoretical ones, but there are much more noise and artifacts in the response functions retrieved. In some results the shape of artifacts are similar to the response of nearby actuators. The results deteriorates compared to previous ones.

It is later found out the the humidity level around the setup is not stable and varies a lot, which would change the ground truth response function of the setup. Another observation is that the laser-camera is also not stable as the error image between shots fluctuates even if the DM is shut off. These factors may lead to the poor performance of the characterization, however it is still up to discussion that each of these factors would infect the characterization to what extend.

A conclusion of this chapter is that, despite the noise and artifacts caused by the unstable setup, the proposed characterization scheme and implemented phase diversity phase retrieval algorithm is capable of characterize a Deformable Mirror (DM). Results of characterization match the theoretical response functions and computation time is shorter than expected.
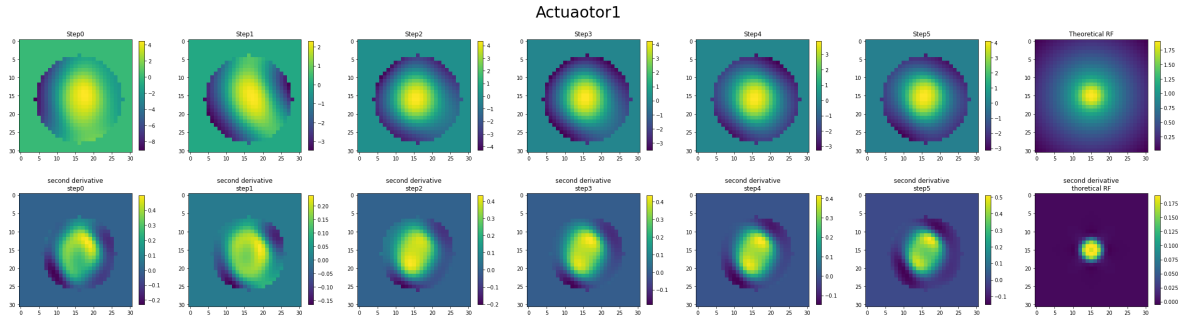
(a) First row: characterization result ϕ_c^1; second row: its second derivative $\nabla^2 \phi_c^1$. Theoretical response function r_1 and $\nabla^2 r_1$ are also shown in the last column.
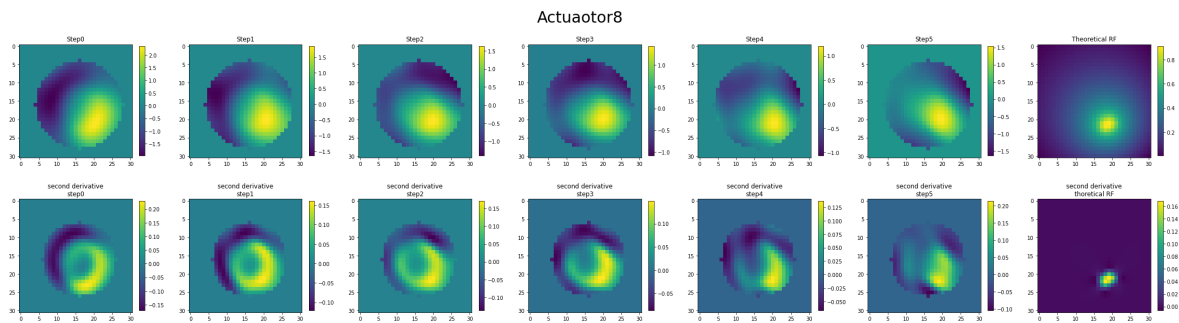
(b) First row: characterization result ϕ_c^8; second row: its second derivative $\nabla^2 \phi_c^8$. Theoretical response function r_8 and $\nabla^2 r_8$ are also shown in the last column.
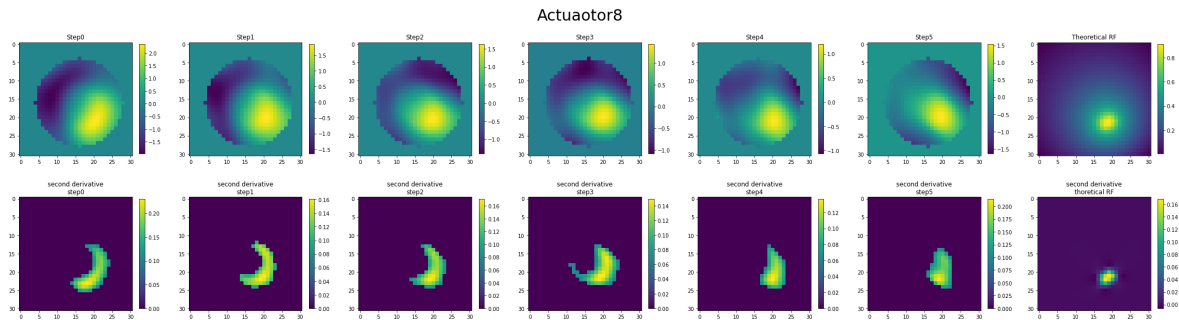
(c) First row: characterization result ϕ_c^8; second row: thresholded $\nabla^2 \phi_c^8$ with threshold value of $12\% \times \max(\nabla^2 \phi_c^8)$. Threshold is used to make the shape of actuator clearer.

Figure 5-10: Second derivative of response functions for actuator #1 and 8. For all other actuators see AppendixA-6 and AppendixA-7.
The second derivative of response function should reveal the shape of corresponding actuator, as shown by theoretical functions r_k and $\nabla^2 r_k$. In characterization results there are artifacts apart from the expected patterns.
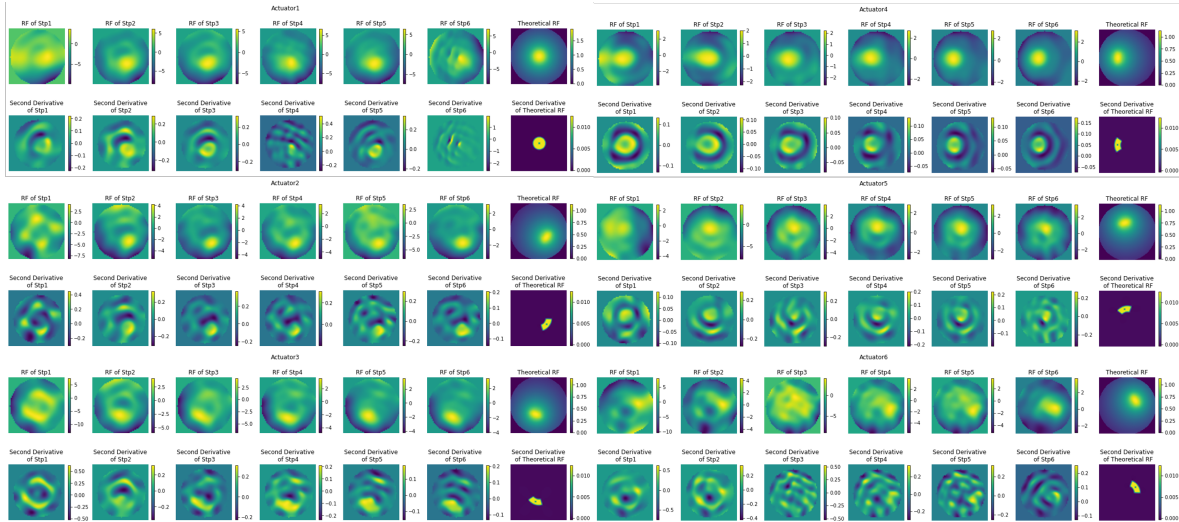
Figure 5-11: Characterization results and second derivative of response functions for actuator#1-17. Actuator #1-17 are the actuators in the first 2 rings of DM. For higher resolution figures see Appendix FigureA-8.
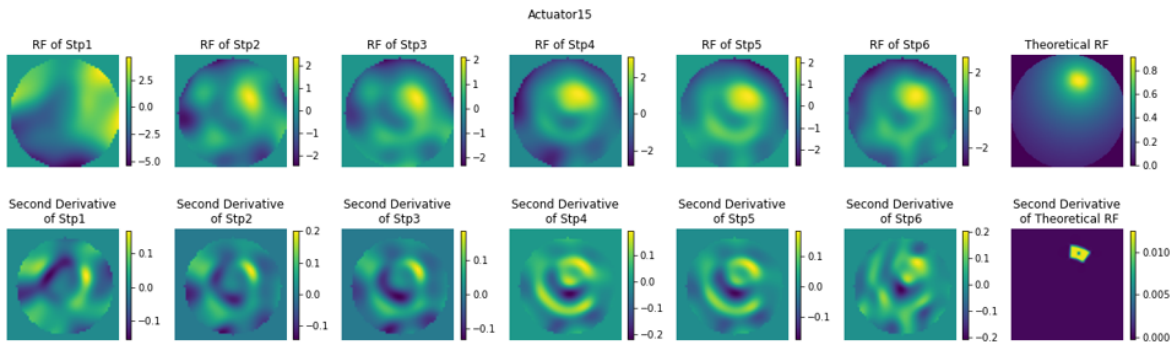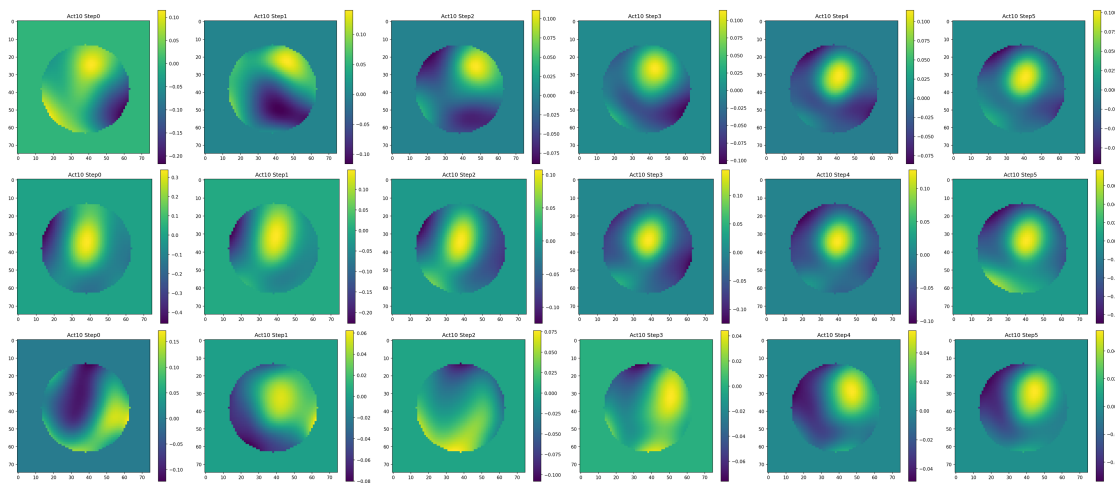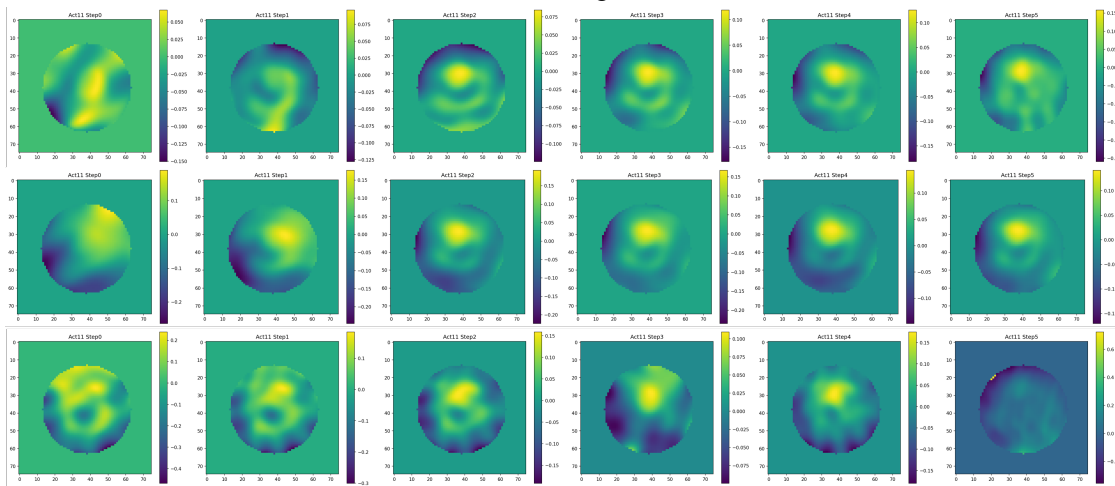

Figure 5-12: Characterization results ϕ_c^{15}, theoretical function r_{15} and second derivatives $\nabla^2\phi_c^{15}, \nabla^2 r_{15}$ of actuator#15.
This example is used to show that with updated configurations, the results are of higher resolution but there are even more noise and artifacts present.

(a) Characterization results actuator #10, run for 3 times with the same configuration and the same initial guess.

(b) Characterization results for actuator #11, run for 3 times with the same configuration and the same initial guess.

Figure 5-13: Example characterizing a same actuator for 3 times.
Ideally the characterization results should remain almost the same for each time. However the obtained response functions vary a lot each time. This indicates that the setup may not be stable.
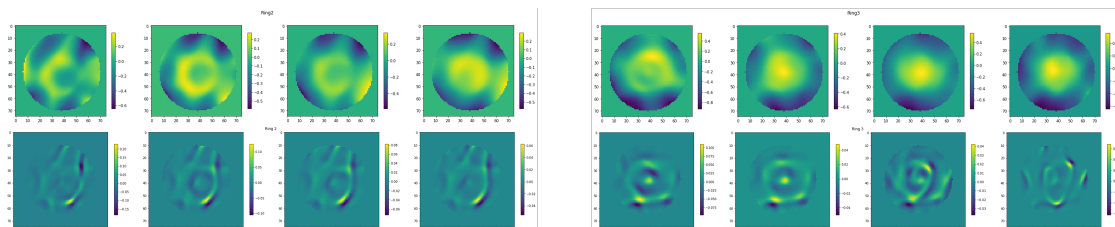
Figure 5-14: Characterization results and second derivative for a whole ring#2(actuator#2-6)(left) and ring#3(actuator#7-17)(right). The shape of rings are vague in the second derivative figures.
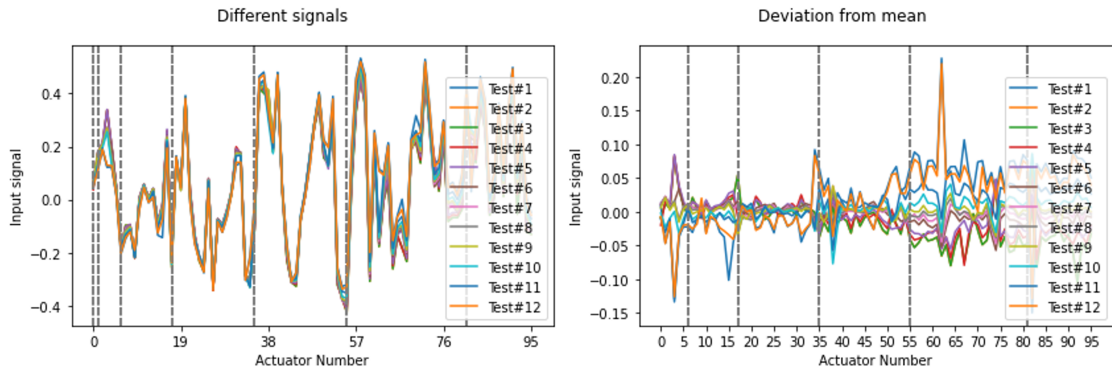
Figure 5-15: Different input signals obtained from optimization that makes the mirror flat. Ideally the "flat" signal should remain almost the same as time changes. However as shown here, the flat signal varies a lot, especially for the first few actuators which are most influential.
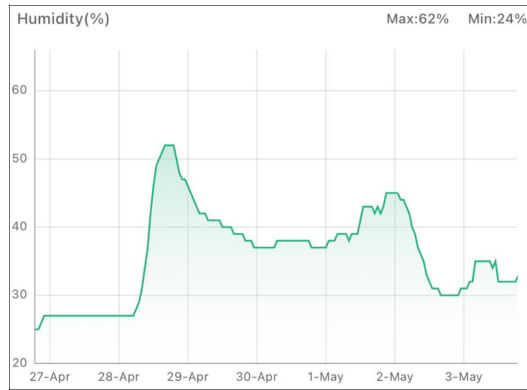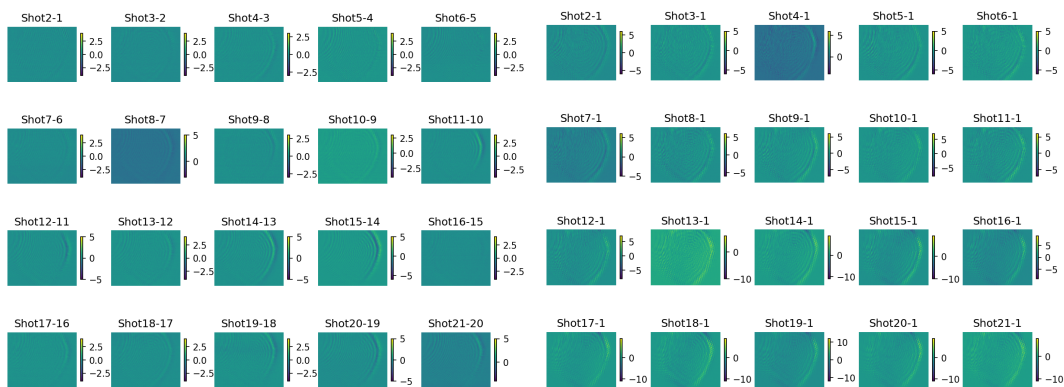

Figure 5-16: Varying humidity level around the setup. Humidity is desirable to remain constant across the characterization process, but it can change up to 40% in a week's time.

(a) Error between 2 neighbouring camera shots, with DM shut off.

(b) Error between camera shots, with DM shut off.

Figure 5-17: Error of camera shots with DM shut off. There should not be any constant patterns for a single mode laser while here the patterns are present.

Chapter 6

Conclusion

From the literature survey it follows that a combination of alternative projection and phase diversity techniques would improve and simplify the WFSless DM characterization process.

Thus, a characterization scheme using GS-based PDPR algorithm, with DM generated phase diversity is proposed. This scheme features using DM to introduce phase diversity and does not require any additional hardware.

To investigate the feasibility of the proposed method, numerical simulations were carried out. A simulation model of the AO setup as well as phase retrieval algorithms are implemented. Using theoretical response functions given by the manufacturer as ground truth, the characterization is performed in simulation. The characterization gives response functions very close to the theoretical ones with RMSE value smaller than 0.02 for most of the actuators. This validates the proposed method and leads to the experiments on a real setup.

Then, in the experimental setup, the characterization is performed for the first 32 actuators. It is then found out that the proposed method is capable of obtain response functions in a much shorter time than expected. However the quality of obtained results are sub-optimal, since there are noise and artifacts present in the response functions.

Seeking results with higher resolutions, the characterization configuration is then modified as padding size for phase increased from 512 to 1024 pixels. Using this configuration the characterization is performed again. However the result of this attempt is worse than expected. More noise and artifacts are presented, which nearly spoiled the results.

It is observed during the characterization that the setup may not be stable, which might be accountable for the sub-optimal results. Issues including DM stability, environmental humidity and unstable laser are addressed and discussed in the end.

In conclusion, the proposed method is capable of characterizing a DM on condition that the setup used is stable throughout time. Simulation results reach an accuracy of ~ 0.02 RMSE for most actuators. Experimental results further validate the method while setup issues are accountable for the sub-optimal performance.
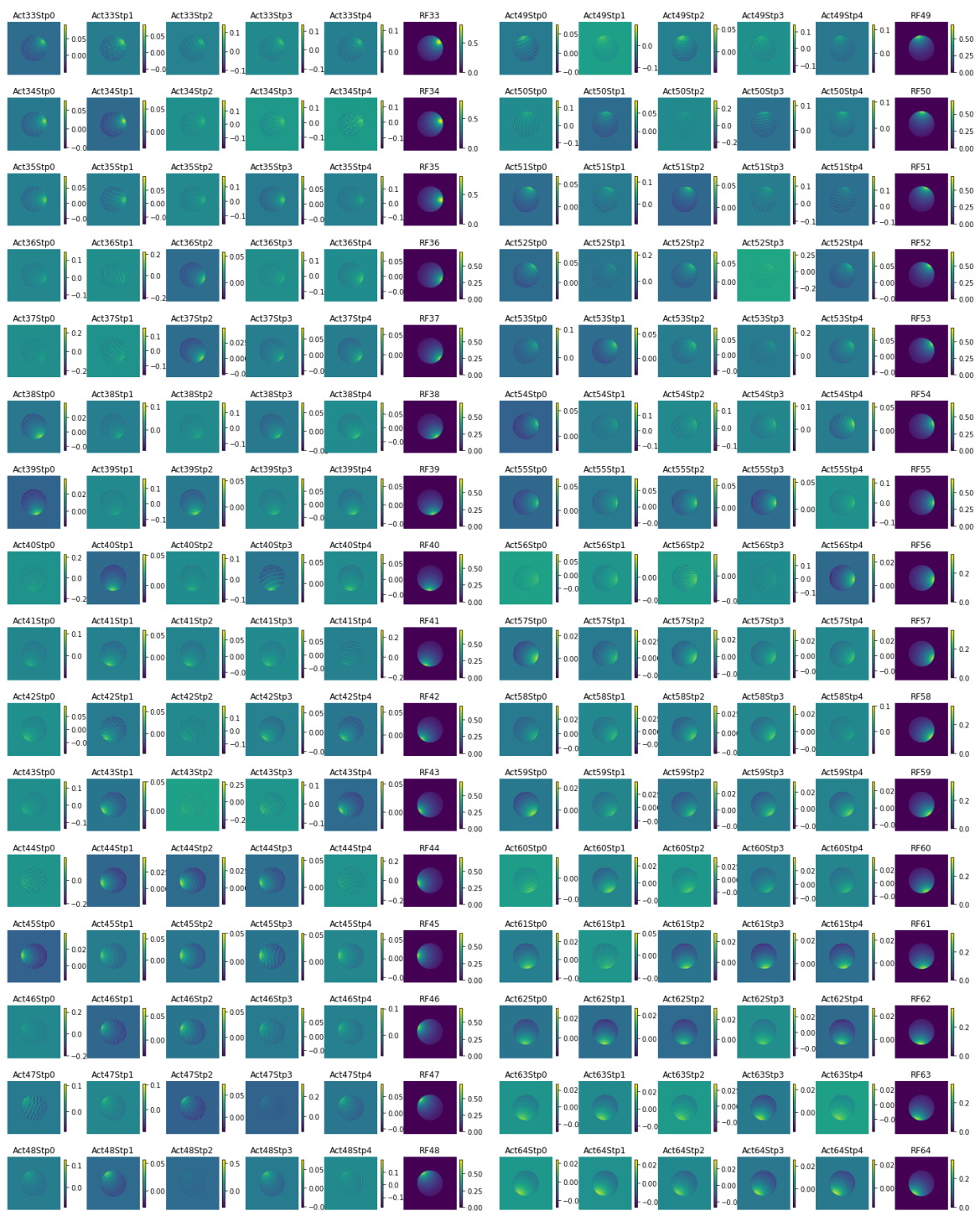
Appendix A

Characterization Results

Phase maps including retrieved response functions and their second derivatives obtained during the thesis.
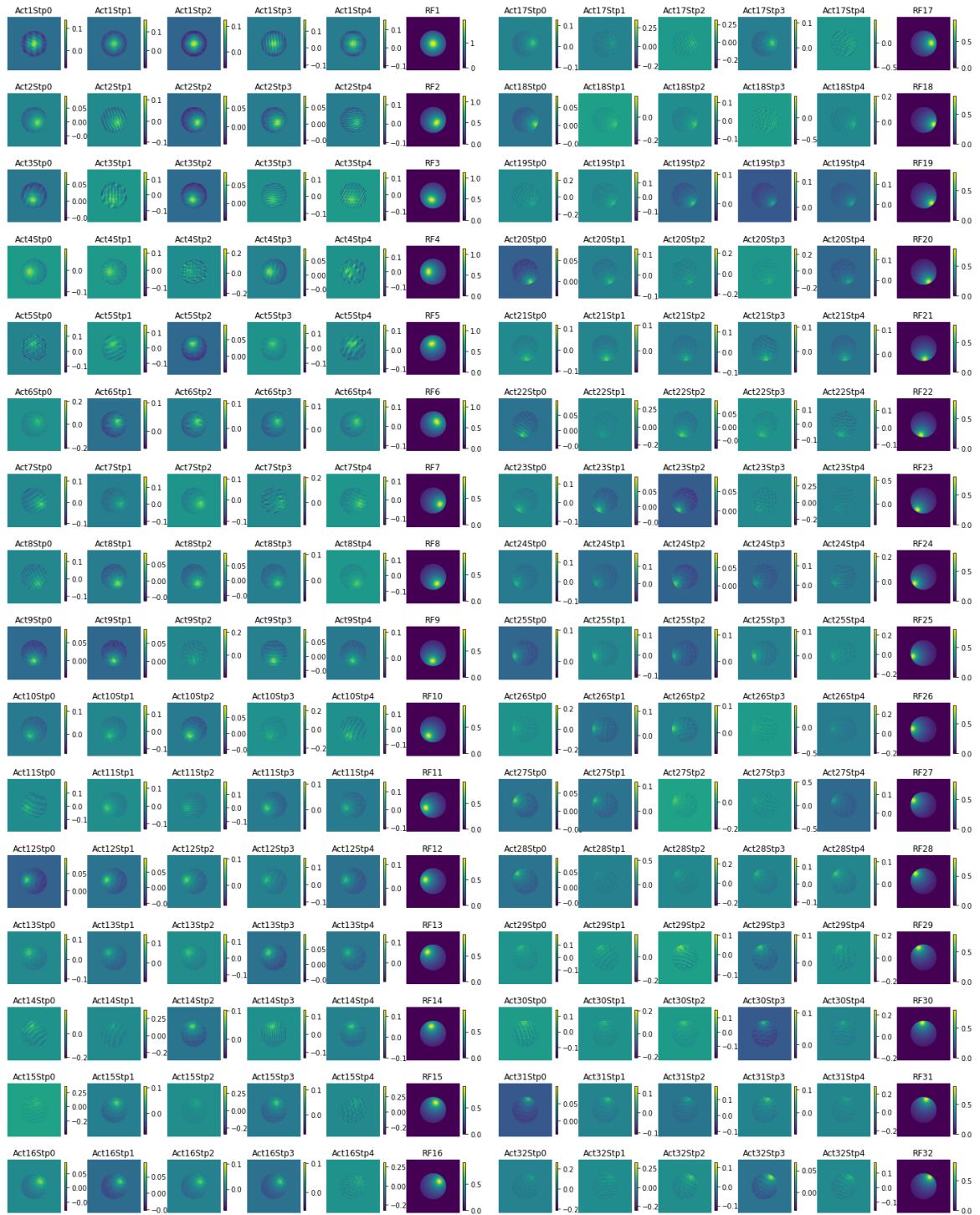
(a) Simulated characterization results for actuator 1-16.

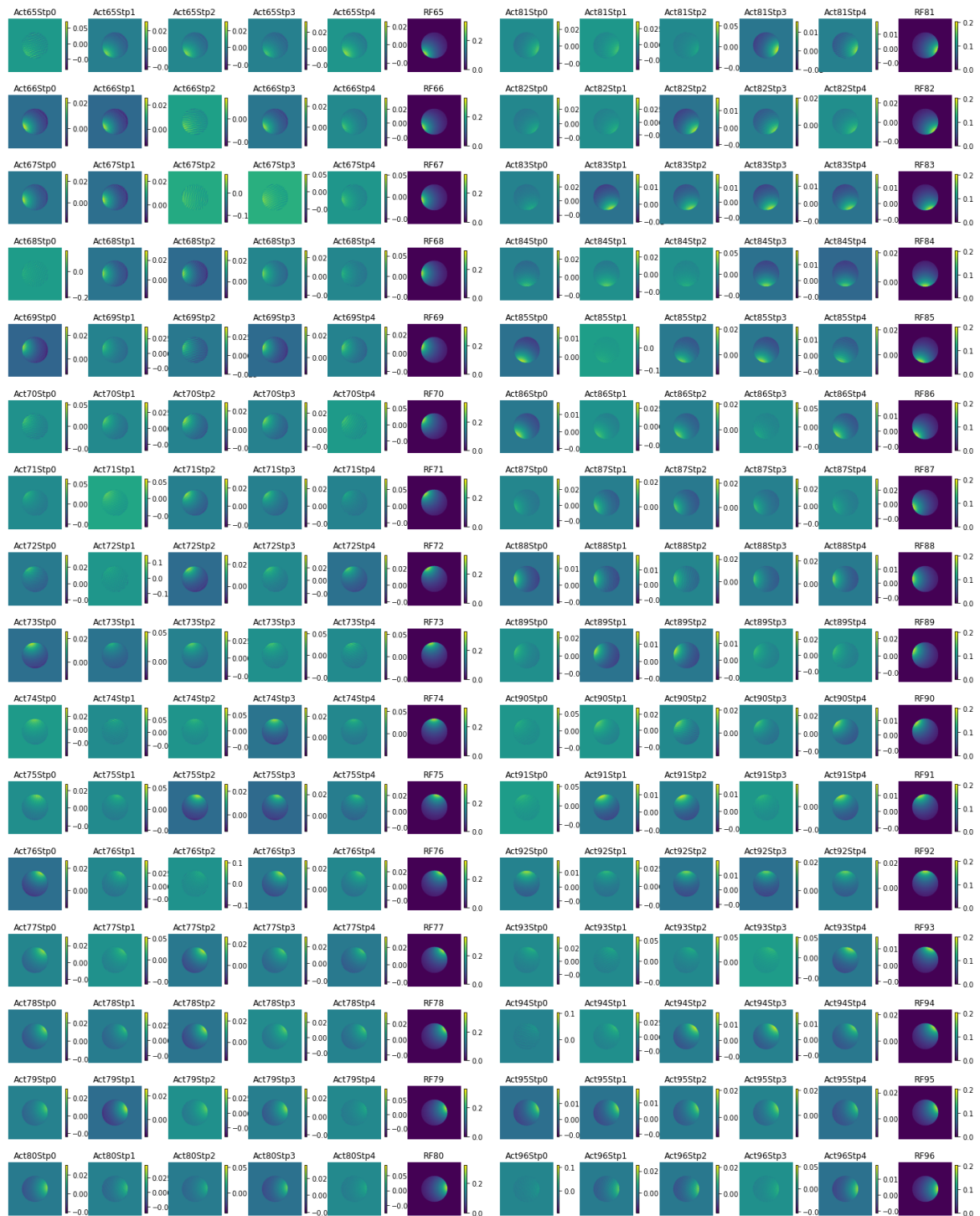(b) Simulated Characterization Results for actuator 17-32.

Figure A-1: Simulated characterization results for actuator 1-32.

(a) Simulated characterization results for actuator 33-48.

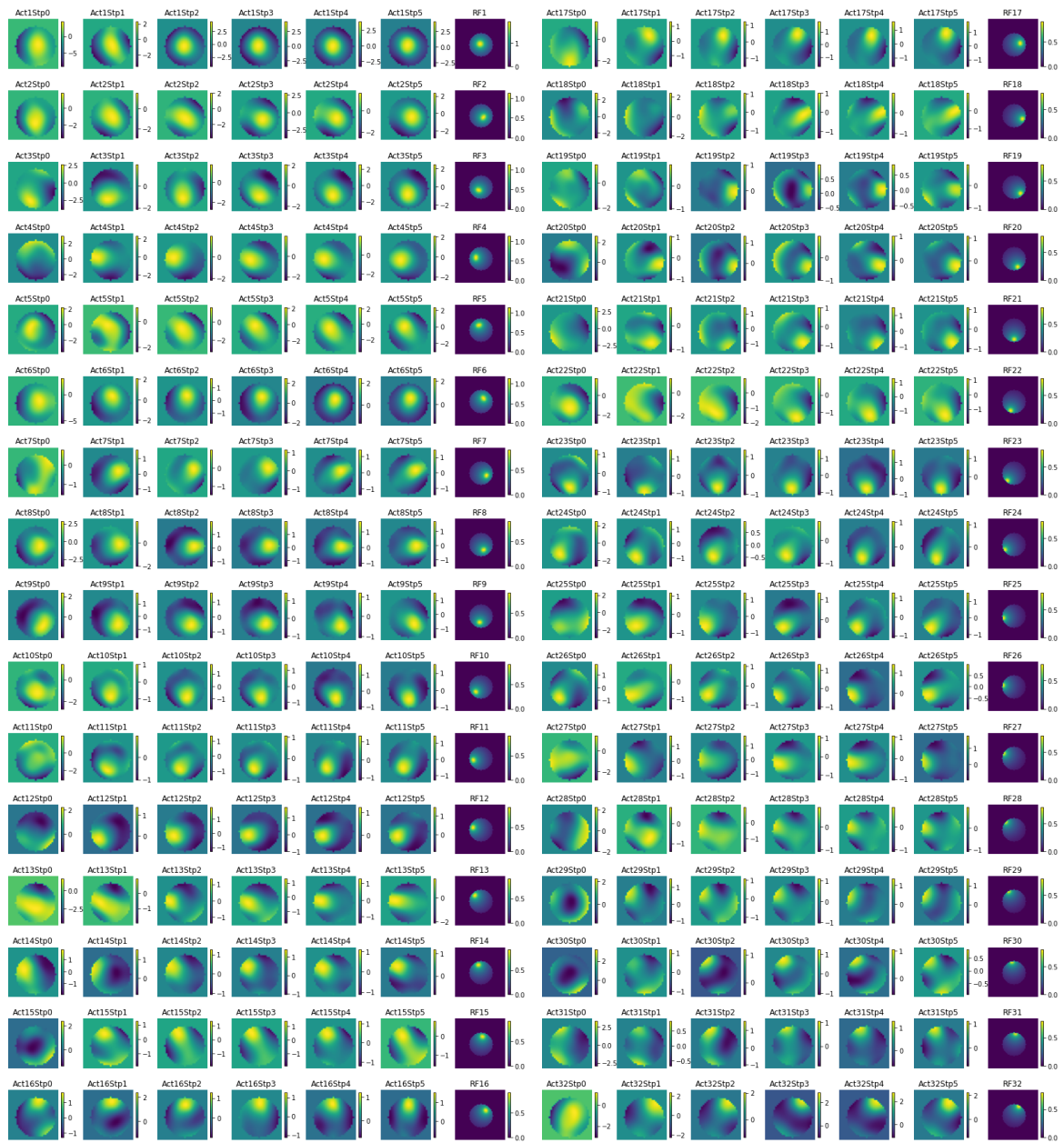(b) Simulated Characterization Results for actuator 49-64.

Figure A-2: Simulated characterization results for actuator 33-64.

(a) Simulated characterization results for actuator 65-80.

(b) Simulated characterization results for actuator 81-96.

Figure A-3: Simulated characterization results for actuator 65-96.

(a) Characterization results for actuator 1-16.

(b) Characterization results for actuator 17-32.

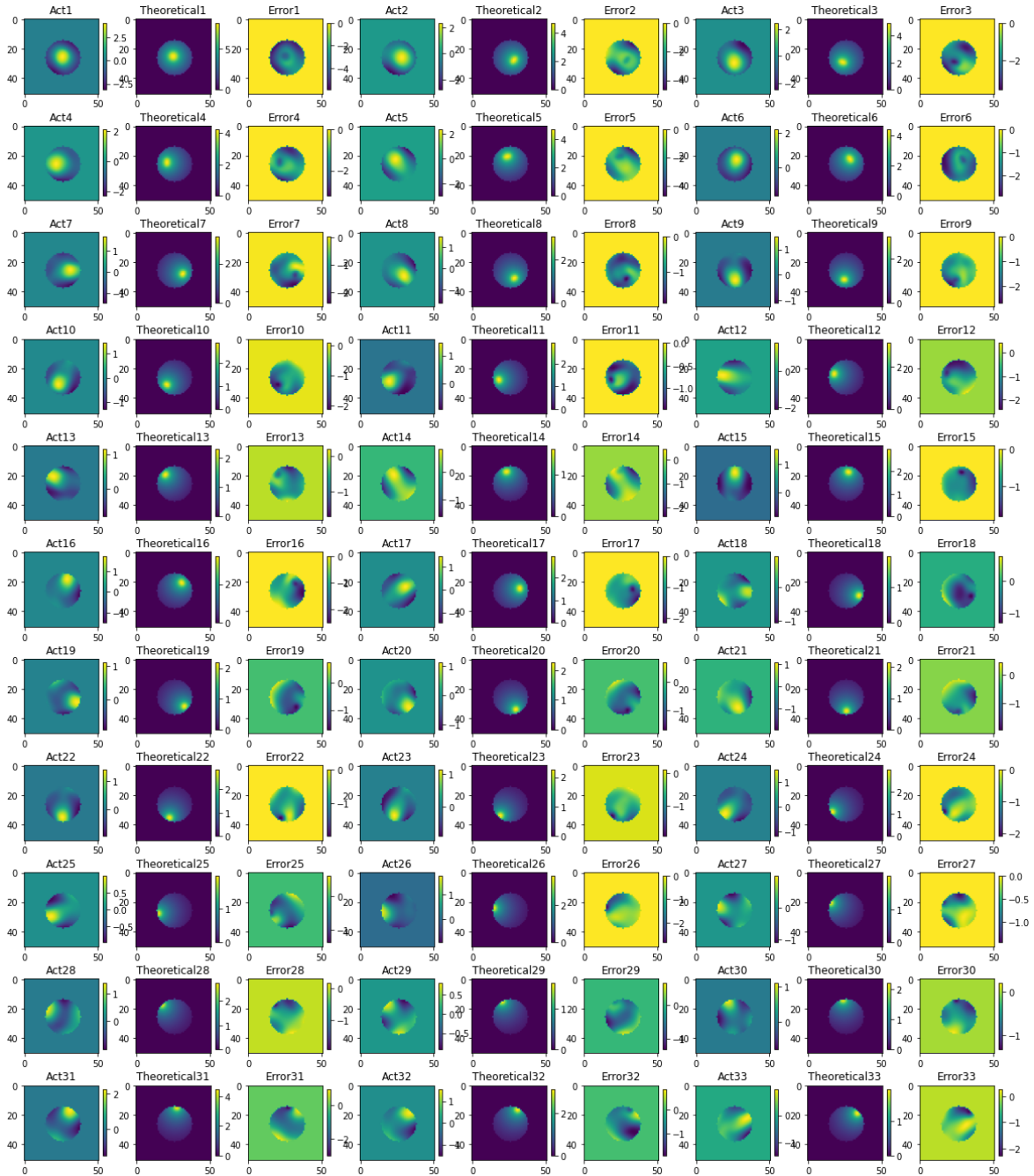**Figure A-4:** Characterization results for actuator 1-32.

Figure A-5: Errors between obtained response functions $\phi_c^k(6)$ and normalized theoretical response $\bar{r}_k$ functions for actuator#1-32. Error phase map shows the misalignment in the setup, as the center of ϕ_c^k sometimes deviates from that in r_k.
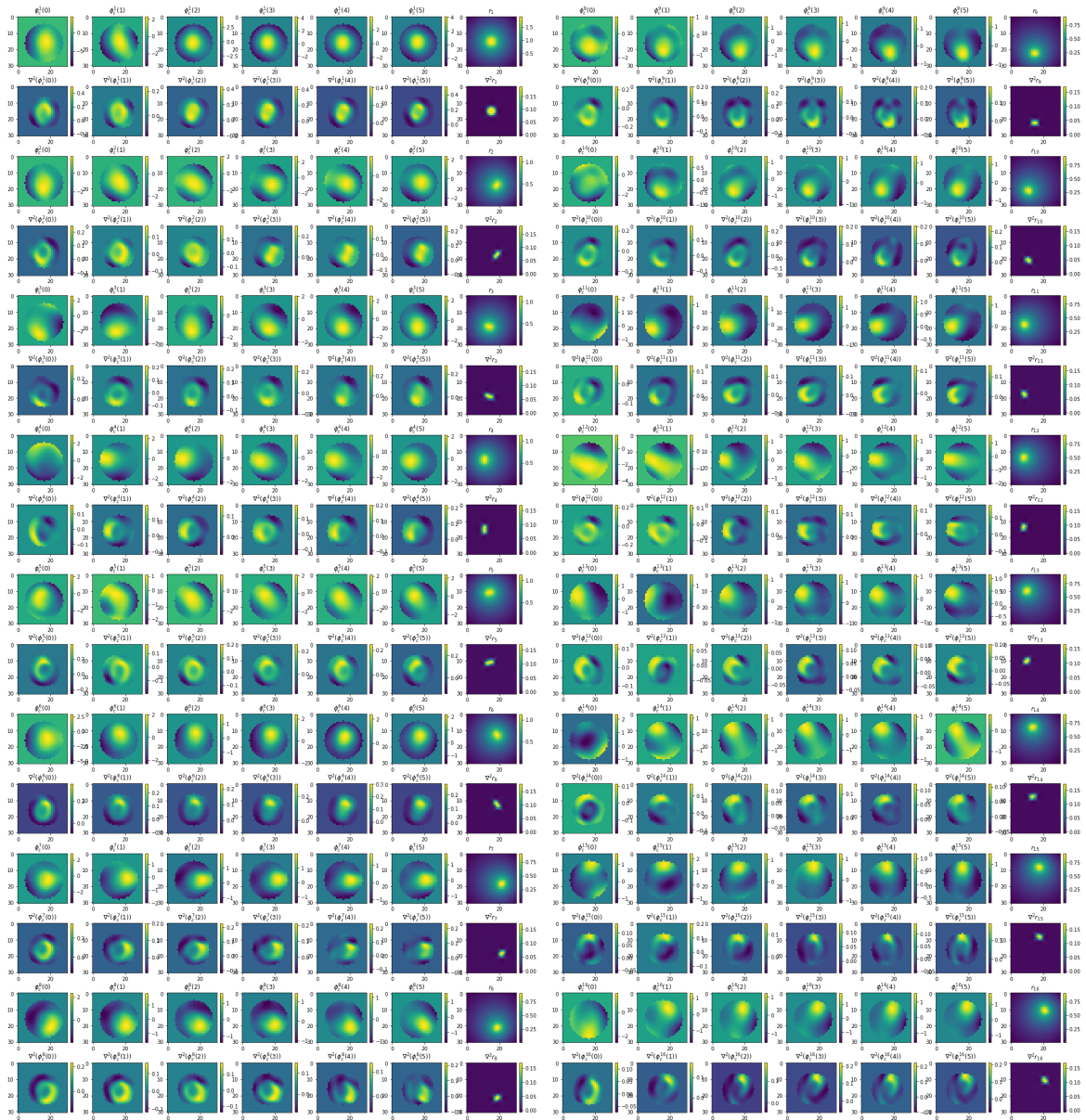
(a) Characterization results and second derivatives of actuator#1-8.

(b) Characterization results and second derivatives of actuator#9-16.

Figure A-6: Characterization results and second derivatives of actuator#1-16.
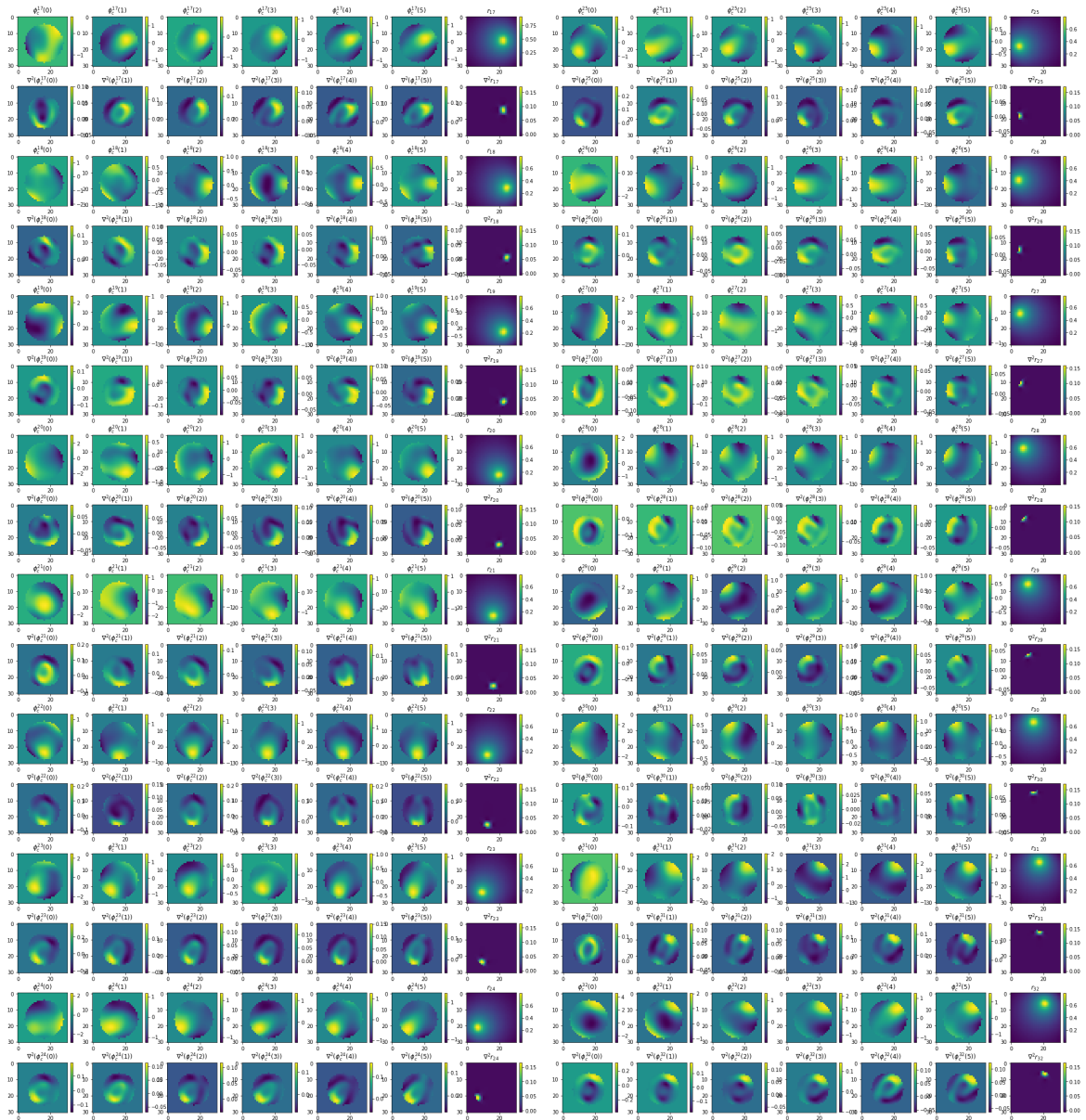
(a) Characterization results and second derivatives of actuator#17-24.

(b) Characterization results and second derivatives of actuator#25-32.

Figure A-7: Characterization results and second derivatives of actuator#17-32.

Figure A-8: Characterization results for actuator 1-17, using larger paddings.
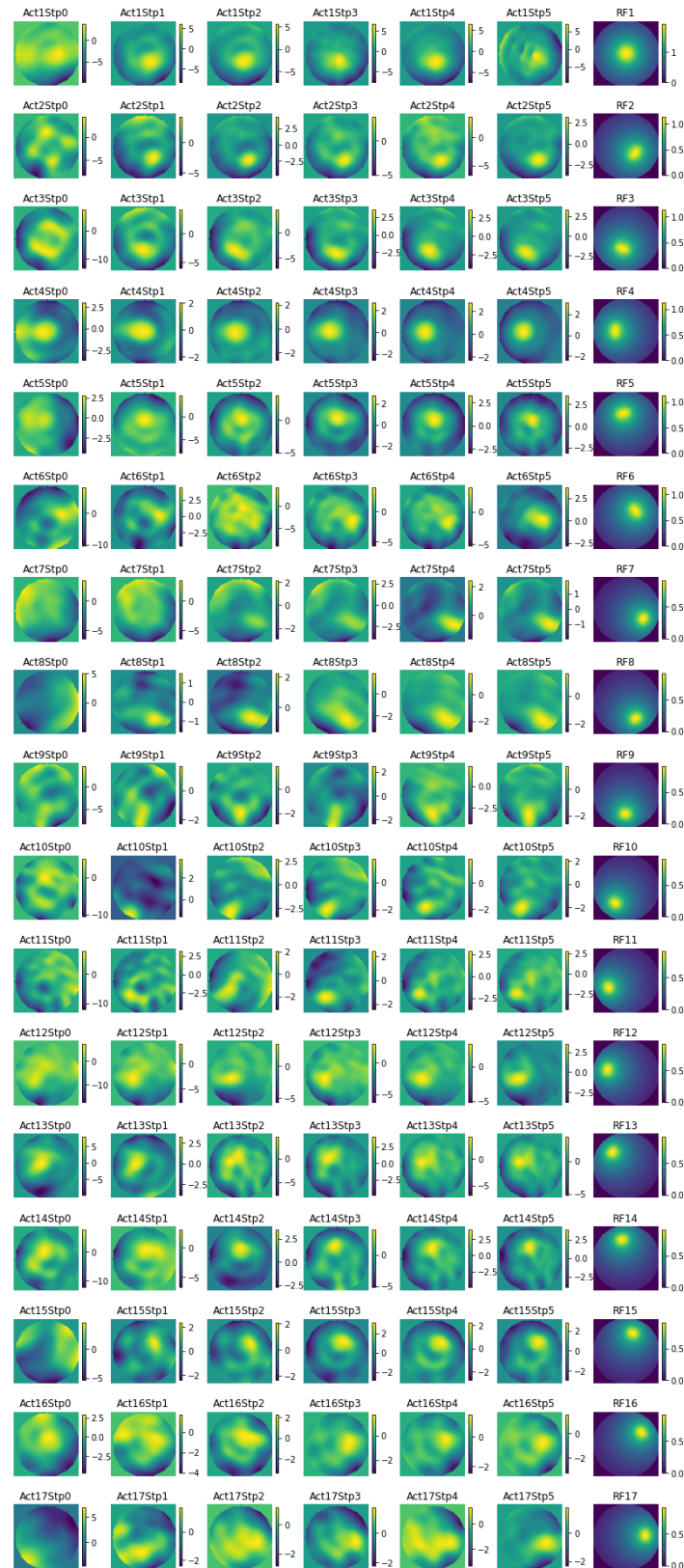
Appendix B

Codes and Algorithms

B-1 Building forward model

```python
def fun_FWsim(input_phasemap,apt,Q):
    """
    Forward Model with fixed auto generated aperture mask for PSF
        simulation
    I/O data:
        input: phasemap, aperture mask, Q value for sampling
        output: Simulated PSF
    """
    # Paramerters from real setup
    psf_sampling = 5.2e-6
    wavelength = 0.632e-6
    aperture_diameter = 0.017
    focal_length = 0.20

    # Q: the ratio of #(pixels in pupil)/#(pixels of aperture)
    # Q = (focal_length * wavelength) / (aperture_diameter * psf_sampling
        )

    # Input phase map
    input_phasemap[np.isnan(input_phasemap)] = 0
    input_phasemap = fun_wrap(input_phasemap)
    img_size = np.shape(input_phasemap)

    # Making pupil plane grids and aperture

    N_pupil = img_size[0]

    # Pixel numer of aperture radius in current configuration
    R_aperture = (N_pupil * Q)/2
```

```
29
30      X_pupil = np.arange(-np.fix(N_pupil/2),np.fix((N_pupil+1)/2),dtype=
            float)
31      Y_pupil = np.arange(-np.fix(N_pupil/2),np.fix((N_pupil+1)/2),dtype=
            float)
32
33      [X,Y] = np.meshgrid(X_pupil,Y_pupil)
34
35      R_pupil = np.sqrt(X**2 + Y**2)
36
37      WF = np.zeros((int(N_pupil),int(N_pupil)))
38      h,w = input_phasemap.shape
39      WF[int(np.floor(N_pupil/2-h/2)):int(np.floor(N_pupil/2+h/2)),int(np.
            floor(N_pupil/2-w/2)):int(np.floor(N_pupil/2+w/2))] =
            input_phasemap
40      WF = WF*apt
41
42      E = np.exp(1j*WF)
43      E[R_pupil>R_aperture]=0
44
45      psf =  abs(fft.fftshift(fft.fft2(E)))**2
46      # Normalize
47      psf = (psf/np.max(psf))
48
49      return psf
```

B-2 Gerchberg-Saxton (GS) algorithm

```
1   def fun_GS(apt, psf_0, max_iter, init_guess, error_threshold):
2       """
3       Gerchberg-Saxton phase retrieval algorithm
4       Input: aperture mask, PSF, maxiter, initial phase guess, error
            threshold
5       output: GS_phase, iter_error, iter_RMSE
6       """
7       p0 = psf_0
8       p0 = np.fft.ifftshift(np.sqrt(p0))
9
10      a = apt
11      a = np.fft.ifftshift(np.sqrt(a))
12
13      # phi = copy.deepcopy(init_guess)
14      phi = init_guess
15      phi = np.fft.ifftshift(phi)
16      # plt.figure(),plt.imshow(np.fft.fftshift(phi)),plt.colorbar(),plt.
            title("Initial Guess")
17
18      phi_0 = np.zeros(np.shape(phi))
19      phi_0 = np.fft.ifftshift(phi_0)
20
21      iter_error = []
22      GS_phase = []
```

```python
23        window = 50
24
25        xx = a * np.exp(phi * 1j)
26
27        iter_RMSE = []
28
29        for iter in tqdm.trange(max_iter):
30
31            X_0 =  np.fft.fft2(xx * np.exp(phi_0 * 1j))
32
33            Y_0 = p0 * np.exp(np.angle(X_0) * 1j)
34
35            y_0 = np.fft.ifft2(Y_0)
36
37            xx = y_0
38
39            iter_error.append(np.linalg.norm(apt * np.exp(phi * 1j) - apt *
                    np.exp(np.angle(xx) * 1j)))
40
41            iter_RMSE.append((np.sqrt(mean_squared_error(fun_crop_fig(phi*apt
                    ,201)  ,fun_crop_fig(np.angle(xx)*apt,201)))))
42
43            phi = np.angle(xx)
44
45            xx = a * np.exp(np.angle(xx) * 1j)
46
47            if iter <= window:
48                if iter_error[iter] < error_threshold:
49                    print('GS algorithm stopped because error threshold has
                            been reached')
50                    print(str(iter) + ' iterations with error threshold of '
                            + str(error_threshold))
51                    GS_phase.append( np.fft.ifftshift(phi)*apt)
52                    return GS_phase, iter_error, iter_RMSE
53
54            if iter > window:
55                if np.mean(iter_error[(iter - window):iter]) <
                        error_threshold:
56                    print('GS algorithm stopped because small improvements in
                            the past 50 iterations')
57                    print(str(iter) + ' iterations with error threshold of '
                            + str(error_threshold))
58                    GS_phase.append( np.fft.ifftshift(phi)*apt)
59                    return GS_phase, iter_error, iter_RMSE
60
61
62            GS_phase.append( np.fft.ifftshift(phi)*apt)
63
64    return GS_phase, iter_error, iter_RMSE
```

B-3   Phase Diversity Phase Retrieval (PDPR) Gerchberg-Saxton (GS) algorithm

```python
def fun_PDPRGS(apt, psf_0, psf_d, phase_d, max_iter, init_guess,
    error_threshold):

    p0 = psf_0
    p0 = np.fft.ifftshift(np.sqrt(p0))

    pd = psf_d
    pd = np.fft.ifftshift(np.sqrt(pd))

    a = apt
    a = np.fft.ifftshift(np.sqrt(a))

    phi = init_guess
    phi = np.fft.ifftshift(phi)
    plt.figure(),plt.imshow(np.fft.fftshift(phi)),plt.colorbar(),plt.
        title("Initial Guess")

    phi_0 = np.zeros(np.shape(phi))
    phi_0 = np.fft.ifftshift(phi_0)

    phi_d = phase_d
    phi_d = np.fft.ifftshift(phi_d)


    PDPR_phase = []
    # window = 50
    window = 10

    xx = a * np.exp(phi * 1j)
    iter_RMSE = []
    iter_error = []

    for iter in tqdm.trange(max_iter):

        X_0 =  np.fft.fft2(xx * np.exp(phi_0 * 1j))
        X_d =  np.fft.fft2(xx * np.exp(phi_d * 1j))

        Y_0 = p0 * np.exp(np.angle(X_0) * 1j)
        # Y_0 = p0 * np.exp((X_0/abs(X_0)) * 1j)

        Y_d = pd * np.exp(np.angle(X_d) * 1j)
        # Y_d = pd * np.exp((X_d/abs(X_d)) * 1j)


        y_0 = np.fft.ifft2(Y_0) * np.exp(-1j * phi_0)
        y_d = np.fft.ifft2(Y_d) * np.exp(-1j * phi_d)

        xx = (y_0+y_d)/2

```

```
48            # error count, do not change order
49            iter_error.append(np.linalg.norm(apt * np.exp(phi * 1j) - apt *
                  np.exp(np.angle(xx) * 1j)))
50            iter_RMSE.append((np.sqrt(mean_squared_error(fun_crop_fig(phi*apt
                  ,201) ,fun_crop_fig(np.angle(xx)*apt,201)))))
51            phi = np.angle(xx)
52            xx = a * np.exp(np.angle(xx) * 1j)
53
54        if iter <= window:
55            if iter_error[iter] < error_threshold:
56                print('GS algorithm stopped because error threshold has
                      been reached')
57                print(str(iter) + ' iterations with error threshold of '
                      + str(error_threshold))
58                PDPR_phase.append( np.fft.fftshift(phi)*apt)
59                return PDPR_phase, iter_error, iter_RMSE
60
61        if iter > window:
62            if np.mean(iter_error[(iter - window):iter]) <
                  error_threshold:
63                print('GS algorithm stopped because small improvements in
                      the past '+str(window)+' iterations')
64                print(str(iter) + ' iterations with error threshold of '
                      + str(error_threshold))
65                PDPR_phase.append( np.fft.fftshift(phi)*apt)
66                return PDPR_phase,iter_error, iter_RMSE
67
68
69        PDPR_phase.append( np.fft.fftshift(phi)*apt)
70
71    return PDPR_phase, iter_error, iter_RMSE
```

Bibliography

[1] Martin J Booth, Delphine Débarre, and Alexander Jesacher. Adaptive optics for biomedical microscopy. *Optics and photonics news*, 23(1):22–29, 2012.

[2] T Fusco, J-M Conan, LM Mugnier, V Michau, and G Rousset. Characterization of adaptive optics point spread function for anisoplanatic imaging. application to stellar field deconvolution. *Astronomy and Astrophysics Supplement Series*, 142(1):149–156, 2000.

[3] Martin Booth, Tony Wilson, Hong-Bo Sun, Taisuke Ota, and Satoshi Kawata. Methods for the characterization of deformable membrane mirrors. *Applied optics*, 44(24):5131–5139, 2005.

[4] Mikhail A Vorontsov, Gary W Carhart, Marc Cohen, and Gert Cauwenberghs. Adaptive optics based on analog parallel stochastic optimization: analysis and experimental demonstration. *JOSA A*, 17(8):1440–1453, 2000.

[5] Huizhen Yang, Oleg Soloviev, and Michel Verhaegen. Model-based wavefront sensorless adaptive optics system for large aberrations and extended objects. *Optics express*, 23(19):24587–24601, 2015.

[6] Yoav Shechtman, Yonina C Eldar, Oren Cohen, Henry Nicholas Chapman, Jianwei Miao, and Mordechai Segev. Phase retrieval with application to optical imaging: a contemporary overview. *IEEE signal processing magazine*, 32(3):87–109, 2015.

[7] M. Verhaegen, P. Pozzi, O. Soloviev, G. Vdovin, and D. Wilding. Control for high resolution imaging. lecture notes, TU Delft, April 2017.

[8] Ariel Lipson, Stephen G Lipson, and Henry Lipson. *Optical physics*. Cambridge University Press, 2010.

[9] Robert K Tyson and Benjamin West Frazier. *Principles of adaptive optics*. CRC press, 2022.

[10] E Scott Claflin and Noah Bareket. Configuring an electrostatic membrane mirror by least-squares fitting with analytically derived influence functions. *JOSA A*, 3(11):1833–1839, 1986.

[11] Michael Shaw, Simon Hall, Steven Knox, Richard Stevens, and Carl Paterson. Characterization of deformable mirrors for spherical aberration correction in optical sectioning microscopy. *Optics express*, 18(7):6900–6913, 2010.

[12] Martin Booth, Tony Wilson, Hong-Bo Sun, Taisuke Ota, and Satoshi Kawata. Methods for the characterization of deformable membrane mirrors. *Applied optics*, 44(24):5131–5139, 2005.

[13] D Russell Luke, James V Burke, and Richard G Lyon. Optical wavefront reconstruction: Theory and numerical methods. *SIAM review*, 44(2):169–224, 2002.

[14] Ralph W Gerchberg. A practical algorithm for the determination of plane from image and diffraction pictures. *Optik*, 35(2):237–246, 1972.

[15] James R Fienup. Phase retrieval algorithms: a comparison. *Applied optics*, 21(15):2758–2769, 1982.

[16] Aharon Levi and Henry Stark. Image restoration by the method of generalized projections with application to restoration from magnitude. *JOSA A*, 1(9):932–943, 1984.

[17] Praneeth Netrapalli, Prateek Jain, and Sujay Sanghavi. Phase retrieval using alternating minimization. *Advances in Neural Information Processing Systems*, 26, 2013.

[18] Jacopo Antonello and Michel Verhaegen. Modal-based phase retrieval for adaptive optics. *J. Opt. Soc. Am. A*, 32(6):1160–1170, Jun 2015.

[19] Runa Briguglio, Marco Xompero, and Armando Riccardi. Optical calibration of large format adaptive mirrors. *arXiv preprint arXiv:2210.04608*, 2022.

[20] Awakash Dixit, Vikash Porwal, and Sanjay Kumar Mishra. Characterization of multi-channel deformable mirror for adaptive optics applications. *Asian Journal of Physics*, 23(4):581–590, 2014.

[21] Anand Sivaramakrishnan and Ben R Oppenheimer. Deformable mirror calibration for adaptive optics systems. In *Adaptive optical system technologies*, volume 3353, pages 910–916. SPIE, 1998.

[22] J Antonello, R Fraanje, H Song, M Verhaegen, H Gerritsen, CU Keller, and T van Werkhoven. Data driven identification and aberration correction for model-based sensorless adaptive optics. In *Optics, Photonics, and Digital Technologies for Multimedia Applications II*, volume 8436, pages 254–262. SPIE, 2012.

[23] Delphine Débarre, T Vieille, and Emmanuel Beaurepaire. Simple characterisation of a deformable mirror inside a high numerical aperture microscope using phase diversity. *Journal of microscopy*, 244(2):136–143, 2011.

[24] Nicholas Hall, Josh Titlow, Martin J Booth, and Ian M Dobbie. Microscope-aotools: a generalised adaptive optics implementation. *Optics Express*, 28(20):28987–29003, 2020.

[25] Mats G Löfdahl, Göran B Scharmer, and Wang Wei. Calibration of a deformable mirror and strehl ratio measurements by use of phase diversity. *Applied Optics*, 39(1):94–103, 2000.

[26] Anisha Thayil and Martin J Booth. Self calibration of sensorless adaptive optical microscopes. *Journal of the European Optical Society-Rapid publications*, 6, 2011.

[27] Bridget M Hanser, Mats GL Gustafsson, DA Agard, and John W Sedat. Phase-retrieved pupil functions in wide-field fluorescence microscopy. *Journal of microscopy*, 216(1):32–48, 2004.

[28] Diwakar Turaga and Timothy E Holy. Image-based calibration of a deformable mirror in wide-field microscopy. *Applied optics*, 49(11):2030–2040, 2010.

[29] Technical passport: 96-channel deformable mirror with embedded electronics. `http://www.okotech.com/images/pdfs/mdm96_25.4_ug.pdf`. Accessed: 2023-05-05.

[30] Details: Ui-1540le-m-gl rev.2. `https://en.ids-imaging.com/download-details/AB02536.html`. Accessed: 2023-05-05.

[31] Alden S Jurling, Matthew D Bergkoetter, and James R Fienup. Techniques for arbitrary sampling in two-dimensional fourier transforms. *JOSA A*, 35(11):1784–1796, 2018.

[32] Justin D Mansell and Brian G Henderson. Temporal and spatial characterization of polymer membrane deformable mirrors. In *Advanced Wavefront Control: Methods, Devices, and Applications VII*, volume 7466, pages 132–141. SPIE, 2009.

Glossary

List of Acronyms

DM	Deformable Mirror
WF	Wavefront
AO	Adaptive Optics
PSF	Point Spread Function
WFSless	Wavefront sensorless
WFS	Wavefront sensor
SVD	singular value decomposition
AP	alternating projection
SDP	semidefinite programming
TIE	transport-of-intensity equation
GS	Gerchberg-Saxton
dOTF	differential optical transfer function
SHWFS	Shack-Hartmann Wavefront Sensor
PD	Phase Diversity
PDPR	Phase Diversity Phase Retrieval
RMS	Rooted Mean Square
SR	Strehl Ratio